Nuclear Engineering and Design 451 (2026) 114830

Contents lists available at ScienceDirect

Nuclear Engineering and Design

journal homepage: www.elsevier.com/locate/nucengdes

Role of bulk condensation in buoyancy-driven gas flows: Insights from THAI HM2 experiment CFD simulations using *containmentFOAM*

Allen George *, Stephan Kelm

Institute of Fusion Energy and Nuclear Waste Management, Forschungszentrum Jülich GmbH, Germany

ARTICLE INFO

Keywords:
Bulk condensation
Classical nucleation theory
Buoyancy-driven flows
Latent heat
ContainmentFOAM
THAI HM2
Fog droplet transport

ABSTRACT

Bulk condensation of steam within a nuclear containment vessel can significantly influence the evolution of pressure, temperature, and gas composition during post-accident transients. Depending on the accident sequence, it can occur at various stages, during which steam is released into the containment under near-saturation conditions. The associated localized latent heat release increases temperature and lowers density, amplifying the buoyancy driven flows that promotes mixing and erosion of stratified light gas layers. Understanding the bulk condensation phenomena interaction is essential for improved containment safety analysis.

Recent developments in *containmentFOAM* CFD package based on OpenFOAM include the implementation and validation of bulk condensation models using saturation-temperature equilibrium (STE) and classical nucleation theory (CNT) approaches. This study presents a comprehensive numerical investigation of the OECD/NEA THAI HM2 benchmark experiment, focusing on bulk condensation influence on multi-component gas mixing dynamics. Steam injection into a pre-stratified vessel atmosphere is simulated with and without bulk condensation model to isolate its effect on hydrogen cloud layer dissolution and gas mixing.

Results indicate that bulk condensation significantly amplifies local buoyancy forces through latent heat release, accelerating vertical flows and hydrogen cloud erosion. The local vertical velocities increases by 15% to 80%, and the hydrogen stratification dissolution occurs 65% faster compared to the simulations without bulk condensation. Strong spatial correlation between bulk condensing zones and enhanced upward flow confirms its decisive role. The simulations show good agreement with experimental temperature and concentration distributions, showing deviations below 10%. Both STE and CNT models predict similar vessel conditions, though CNT provides a more physical representation of fog volume and droplet size distributions. These findings highlight the vital role of bulk condensation in driving containment atmosphere mixing, with direct implications for hydrogen risk mitigation strategies.

1. Introduction

The safety of the environment surrounding a nuclear power plant relies on the integrity of containment structure during accident conditions. In the event of an accident, such as a loss of coolant accident (LOCA), which may progress to a severe accident involving significant core degradation, large quantities of steam and hydrogen may be released into the containment atmosphere (Gupta et al., 2025; Paladino et al., 2022; IAEA, 2011). This can lead to the formation of stratified hydrogen layer in the upper zones of the containment vessel. Local hydrogen accumulations at elevated temperature and pressure pose significant risk due to its wide flammability range and potential to undergo rapid combustion. Simultaneous events inside the containment, such as steam release, can generate buoyancy- and momentum-driven flows that interact with and erode existing stratified layers. Past accidents like the Fukushima Daiichi accident (NEA, 2011; IAEA, 2015) have shown the consequences of hydrogen explosion, highlighting the need for focus on hydrogen management and mitigation strategies in nuclear safety research. The threat of containment failure resulting from severe accidents underscores the critical need to thoroughly understand the phenomena occurring within the containment under these extreme conditions.

The containment atmospheric conditions are governed by the interaction between several thermal hydraulic phenomena, including turbulence, multicomponent gas transport, buoyancy, condensation, as well as conjugate and radiation heat transfer processes. Among these, condensation plays a major role in mitigating the pressure buildup and temperature rise within the containment. As steam gets released

* Corresponding author.
E-mail addresses: a.george@fz-juelich.de (A. George), s.kelm@fz-juelich.de (S. Kelm).

https://doi.org/10.1016/j.nucengdes.2026.114830
Received 19 September 2025; Received in revised form 16 December 2025; Accepted 7 February 2026
Available online 17 February 2026

Nomenclature

α_f	Fog volume fraction
β	Condensation coefficient
Δt	Time step size (s)
$\dot{m}'''_{bulk}$	Bulk condensation volumetric rate (kg/m^3)
$\dot{m}''_{wall}$	Wall condensation mass flux (kg/m^2)
$\dot{r}$	Droplet growth rate (m/s)
λ	Thermal conductivity of gas mixture ($W/(m\,K)$)
λ_s	Thermal conductivity of solid material($W/(m\,K)$)
μ	Dynamic viscosity of gas mixture ($kg/(m\,s)$)
ν	Kinematic viscosity of gas mixture (m^2/s)
ν_t	Turbulent eddy viscosity of gas mixture (m^2/s)
ω	Turbulence dissipation of gas mixture (1/s)
ρ	Density of gas mixture (kg/m^3)
ρ_f	Density of fog (kg/m^3)
ρ_s	Density of solid material (kg/m^3)
σ	Surface tension (N/m)
τ	Viscous stress tensor ($kg/(m^1\,s^2)$)
τ_{fog}	Fog droplet relaxation time (s)
$\vec{g}$	Gravitational acceleration vector (m/s^2)
$\vec{n}_{wall}$	Unit vector normal to wall
$\vec{S}_U$	Momentum source term ($kg/(m^2\,s^2)$)
$\vec{U}$	Velocity of gas mixture (m/s)
$\vec{U}_d$	Drift velocity of fog droplet (m/s)
$\vec{U}_{wall}$	Condensation suction velocity (m/s)
C_p	Specific heat capacity of gas mixture(J/K)
C_d	Drag coefficient
$C_{p,s}$	Specific heat capacity of solid material (J/K)
d_f	Fog droplet diameter (m)
$D_{j,m}$	Molecular diffusivity of the jth is the species in the mixture (m^2/s)
d_{mean}	Fog droplet mean diameter (m)
D_t	Turbulent diffusivity of gas mixture (m^2/s)
h	Static enthalpy of gas mixture (J/kg)
h_j	Specific enthalpy of jth species (J/kg)
h_{lg}	Latent heat of vaporization of steam (J/kg)
I	Nucleation rate ($1/(m^3\,s)$)
K	Specific kinetic energy of gas mixture (J/kg)
k	Turbulent kinetic of gas mixture (m^2/s^2)
N	Number of species
N_A	Avogadro constant (1/mol)
p	Pressure (Pa)
p_{H_2O}	Partial pressure of steam species in gas mixture (Pa)
p_{sat}	Saturation pressure of steam (Pa)
Pr_t	Turbulent Prandtl number
R	Universal gas constant (J/(mol K))
r_{cr}	Critical nucleation radius (m)
S_j	Specie mass source term ($kg/(m^3\,s)$)
S_m	Mass source term ($kg/(m^3\,s)$)
S_h	Energy source term (W/m^3)
$S_{m,f}$	Fog mass source term ($kg/(m^3\,s)$)
Sc_t	Turbulent Schmidt number
st	Degree of supersaturation
T	Temperature of gas mixture (K)
t	Time (s)
T_s	Temperature of solid material (K)
T_{sat}	Saturation temperature of steam (K)
W	Molar mass of gas mixture (kg/mol)
W_k	Molar mass of kth species (kg/mol)
Y_j	Mass fraction of jth species
BPG	Best practice guidelines
CFD	Computational fluid dynamics
CHT	Conjugate heat transfer
CNT	Classical nucleation theory
GCI	Grid Convergence Index
ISP	International standard problem
LOCA	Loss of coolant accident
STE	Saturation temperature equilibrium
URANS	Unsteady Reynolds-Averaged Navier–Stokes

into the containment, it may condense either on the surfaces of cold internal structures (wall condensation) as drops, rivulets or films, or in volume (bulk condensation) as fog droplets. Bulk condensation is often neglected in containment analysis due to its lower contribution to overall water/steam mass and heat balance compared to wall condensation. However, bulk condensation, due to its localized nature, can have a strong impact on the gas mixing dynamics especially in buoyancy-driven flows. The latent heat released to the gas during bulk condensation raises the local gas temperatures, leading to the decrease in the gas density at those locations. This can generate localized buoyancy forces strong enough to accelerate vertical gas mixing and breakdown of any stratification layers. Bulk condensation and the associated fog formation can occur in reactor containments during LOCA when steam is released into a colder containment atmosphere, whose temperature is lower than the steam saturation temperature. This phenomenon was addressed as part of the ISP-47 study (Allelein et al., Sep 2008), with its effects examined in detail through the THAI experimental program. The THAI HM2 experiment (Kanzleiter et al., 2008), derived from ISP-47 by including better instrumentation, provides an idealized benchmark for investigating bulk condensation and its coupling with buoyancy-driven gas transport under containment conditions. In phase 2 of the HM2 test, a stratified hydrogen-nitrogen atmosphere at the upper zone was subjected to controlled high-temperature steam injection from the lower, resulting in the complex interactions between condensation, buoyancy and gas mixing. The experiment's extensive, high-resolution measurements of vessel pressure, local temperature, and gas concentrations enable detailed analysis of vessel conditions and comparison with numerical simulations, although direct measurements of fog distribution were not explicitly available. Previous HM2 simulation studies (Royl et al., 2008; Visser et al., 2014; Schwarz et al., 2011) have extensively benchmarked and validated the ability computational fluid dynamics codes – such as FLUENT, GASFLOW, and GOTHIC – to predict hydrogen stratification and dissolution in THAI HM2 experiment. The blind calculations (Royl et al., 2008) exhibited large variations in predicting dissolution dynamics, particularly the timing and extent of cloud erosion. Visser et al. (2014) demonstrated that hydrogen stratification and dissolution prediction in THAI HM2 improved through proper mesh resolution and inclusion of buoyancy effects in turbulence modeling. Schwarz et al. (2011) emphasized that CFD accuracy depends on correct turbulence modeling, wall treatments, bulk condensation, and fog settlement–omitting the latter generates unphysical plume buoyancy.

Accurate modeling of bulk condensation and its interaction with other phenomena can improve the prediction of containment conditions which is essential for designing effective safety systems. Traditional lumped-parameter system codes, while useful for global assessments, often lack spatial resolution necessary to capture local flow,

mixing and heat transfer effects that are critical during accident scenarios. Computational fluid dynamics (CFD) has emerged as a powerful tool, offering the ability to resolve three-dimensional flow structures, local temperature and concentration gradients — capabilities which are particularly important for analyzing bulk condensation scenarios, where localized effects play a crucial role. Previous CFD studies have modeled bulk condensation effects using a range a approaches, from simple single-phase Eulerian method where condensed fog disregarded as a mass sink (Vyskocil et al., 2014 using ANSYS Fluent), to more detailed two-phase Eulerian-Eulerian method considering fog droplet-gas interactions (Zhang and Laurien, 2014 using ANSYS CFX), Eulerian-Lagrangian method for fog droplet tracking (Babić et al., 2009 using ANSYS CFX) and, and spray droplet bulk condensation simulations using CMFD codes (Kaltenbach and Laurien, 2018; Mimouni et al., 2010). The present work employs OpenFOAM based CFD package called *containmentFOAM* (Kelm et al., 2021), which is equipped with validated models essential for containment thermal-hydraulic simulations, including multi-species transport, turbulence transport in buoyancy affected flows (Kampili et al., 2021), conjugate heat transfer, radiation heat transfer (Liu et al., 2022), wall condensation (Vijaya Kumar et al., 2021), and bulk condensation with fog droplets transport (George et al., 2023). In addition to these established capabilities, this study implements a new bulk condensation model based classical nucleation theory approach (Sidorov and Yastrebov, 2023) within the *containmentFOAM* framework, and a comparative analysis of the different bulk condensation models is conducted.

The objective of this study is to address the role of bulk condensation in buoyancy flows and multi-component gas mixing within a containment during accident scenarios, using THAI HM2 experiment. The evolution of the vessel pressure, local temperature and hydrogen distributions from simulations using containmentFOAM are analyzed in detail to understand how latent heat release during bulk condensation affects buoyancy driven flow and the erosion of the hydrogen-rich stratified layer. Simulations are conducted both with and without bulk condensation models, as well as with two different bulk condensation models, to clearly isolate and quantify its impact on the transient gas composition and temperature distributions within the vessel. The simulation results are compared against experimental data from THAI HM2 test to assess the accuracy of the findings and validate the modeling approach. This work aims to understand the need to include bulk condensation models into containment CFD models for reliable prediction of containment atmospheric conditions during accident scenarios.

2. THAI HM2 experiment

The HM2 experimental test (Kanzleiter et al., 2008) was conducted at THAI facility operated by Becker Technologies GmbH, Germany. The facility comprises a cylindrical stainless steel vessel of 9.2 m height and 3.2 m diameter with a total internal volume of 60 m^3 (Fig. 1). The vessel comprises an inner wall which 22 mm thick, followed by a 16.5 mm thick thermal oil (coolant) gap and a 6 mm thick outer wall, all covered by a 120 mm rockwool for thermal insulation. There is a coolant circuit that is present only in the cylindrical region of the vessel, but it is not operated during the HM2 experiment, leaving the oil remaining stagnant. The internal structures include an inner cylinder, which is completely open at its upper and lower ends, and four lateral condensate trays that obstruct the flow in the annulus region with a blockage ratio of 0.67. The inner cylinder is 4.1 m long, 10 mm thick, and has an outer diameter of 1.4 m. The HM2 test focuses on gas distribution processes within the vessel, particularly investigating the formation of hydrogen cloud in the upper section and its gradual dissolution by steam injection from the lower section. The vessel is first purged by nitrogen injection through the bottom valve while keeping the relief valve at the top open. Once the purging is complete, both valves are closed, resulting in a vessel pressure of 1 bar and mean gas temperature is 21 °C. Afterwards, hydrogen is injected at a rate of 0.3 g/s for a period of 4200 s (phase 1) into the vessel through a vertical pipe in the upper annulus region with outlet level at height of 4.8 m. This leads to the formation of a hydrogen cloud (≈ 40 vol%) in the upper section and increases the vessel pressure to 1.26 bar and mean temperature to approximately 22 °C. Next, steam is released into the vessel at 24 g/s for a duration of 2500s (phase 2) by a vertical nozzle located at the central axis of the vessel at height 1.8 m. The released steam first passes through the inner cylinder and then starts to break down the hydrogen-nitrogen cloud in the dome from below. Steam condensation will take place simultaneously both within the bulk and on the surfaces of the inner cylinder as well as the main vessel's inner walls. By the end of the steam injection phase, the vessel pressure increases to 1.45 bars. Finally, during the last phase (duration ≈ 1000 s), there is no gas injection, allowing the gas mixture to settle and calibration of gas concentration measuring system performed. During this period, the vessel pressure decreases to around 1.32 bars, resulting from further condensation of steam.

The facility was equipped with an extensive measurement system to measure the gas injection rates and to capture the detailed evolution of temperature, pressure, and gas composition throughout the experiment. The hydrogen and steam mass flow rates during their injection periods were measured with a rotameter type transducer with an accuracy of 2%. The hydrogen concentration at different heights of the vessel was continuously monitored by dedicated gas sampling lines and analyzing them with a heat conductivity sensor. Multiple calibrated thermocouples were used to monitor gas and wall temperatures at various heights and circumferential locations. The evolution of the total pressure in the test vessel was determined using two strain-gauge transducers which were backed up by high-precision manometer readings. These measurement data enable a detailed comparison between the events occurring inside the vessel during the experiment and those predicted by the numerical model, facilitating an analysis of how bulk condensation influences the thermal-hydraulic behavior, gas mixing, and stratification erosion in the containment atmosphere. Direct measurements of wall condensate flow or fog droplet distribution were not available in the HM2 experiment. The locations of the hydrogen concentration sampling points and temperature thermocouples relevant to this study are illustrated in Fig. 1. The hydrogen concentration sensors are positioned at a radial distance of around 1 m in the annular region, while the temperature sensors are located at a radial distance of 0.35 m within the inner cylinder region. Since the primary focus of this work is the effect of bulk condensation, simulations are limited to phases 2 and 3 of the experiment.

3. Modeling approach

The numerical modeling framework in this study is based on *containmentFOAM*, which solves the unsteady Reynolds-Averaged Navier–Stokes (URANS) equations using a single-phase approach for multi-component gas mixtures. The governing equations are formulated for the gaseous phase, with condensation phenomena coupled through mass transfer terms that modify these conservation equations. Wall condensation is accounted by imposing mass outflux through the wall boundaries, whereas bulk condensation in the gas volume is modeled using volumetric mass source or sink terms within the computational domain. The fog droplets generated during bulk condensation are transported as a passive scalar that can undergo re-evaporation or get deposited on wall surfaces. The gas flow field turbulence is resolved employing the standard $k-\omega$ SST turbulence model (Menter and Esch, 2001), with additional production and dissipation terms to account buoyancy influences in the turbulent kinetic energy and the turbulence dissipation equations (Kampili et al., 2021). The gas mixture properties are derived from the individual species properties; dynamic viscosity (μ) and thermal conductivity (λ) are calculated using Wilke's mixture law (Wilke, 1950), while specific heat capacity (C_p) is obtained by mass-weighted averaging. The thermophysical properties

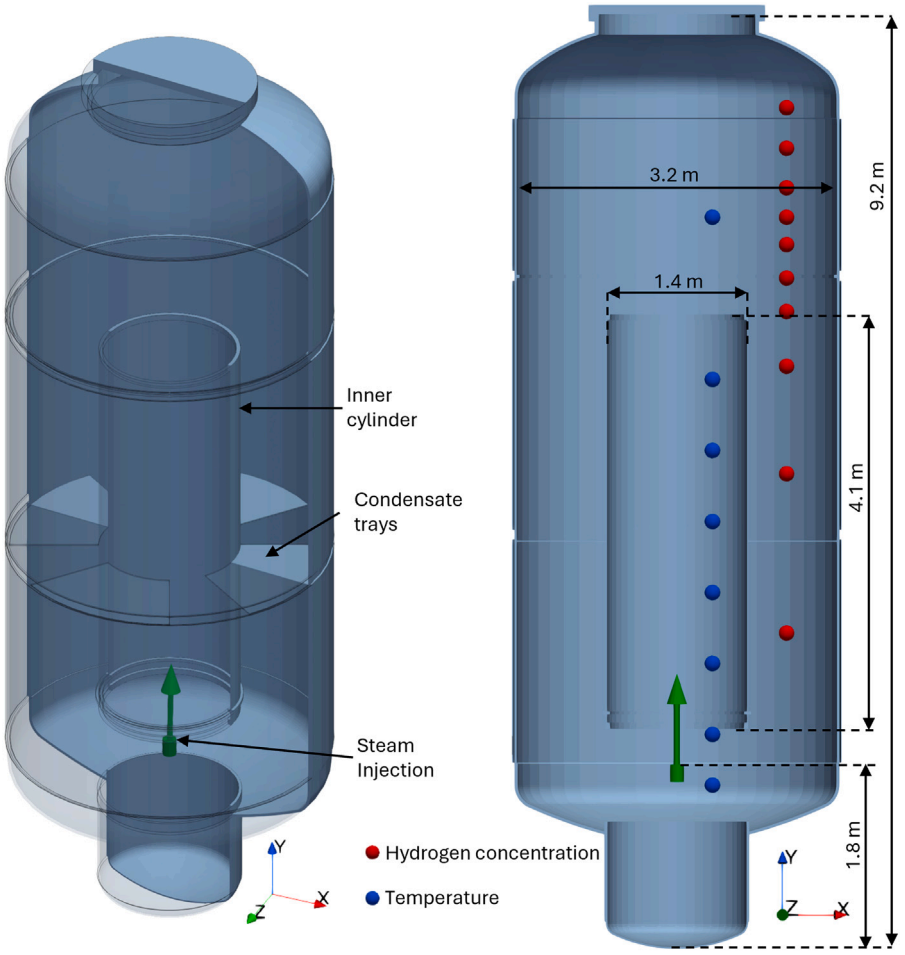

Fig. 1. HM2 experiment vessel schematic, and temperature and hydrogen concentration measurement locations.

of each species are derived from second order polynomial fits to the data from NIST Chemistry Webbook (Linstrom and Mallard, 2025). The effective diffusivity of each species in the gas mixture is determined according to Fick's law, utilizing binary diffusion coefficients of each pair of species obtained through Fuller's model (Fuller et al., 1966). The development and implementation *containmentFOAM* models, along with its validation from small-scale separate effect tests to large scale containment applications, are summarized in Kelm et al. (2021).

3.1. Governing equations

The following conservation equations form the basis of the overall modeling approach:

3.1.1. Total mass conservation equation

$$\frac{\partial \rho}{\partial t} + \nabla \cdot (\rho \vec{U}) = S_m \tag{1}$$

where ρ is the density of the multi-component gas mixture and $\vec{U}$ is its velocity, The term S_m accounts for the mass sink (or source) arising from condensation (or evaporation).

3.1.2. Species mass conservation equation

The containment atmosphere consists of a mixture of N gas species, typically including N_2, O_2, H_2 and H_2O. The transport equations are expressed in terms of specie mass fraction (Y_j):

$$\frac{\partial \rho Y_j}{\partial t} + \nabla \cdot (\rho \vec{U} Y_j) = \nabla \cdot \left[\rho \left(D_{j,m} + D_t\right) \nabla Y_j\right] + S_j \tag{2}$$

where $D_{j,m}$ is the molecular diffusivity of the jth is the species in the mixture. The turbulent diffusivity is obtained from the turbulence model using the relation $D_t = \nu_t / Sc_t$, where ν_t is the eddy viscosity and $Sc_t = 0.85$ is the turbulent Schmidt number. The S_j term accounts for the mass sink, which is generally zero for all species except for steam, when condensation or evaporation occurs. The summation of N species equations gives the total mass conservation equation (Eq. (1)). In *containmentFOAM*, $N - 1$ species equations are solved along with the total mass conservation equation and the mass fraction of the Nth species (abundant non-condensable gas) is determined from the mass fraction constraint relation, $\sum_{j=1}^{N} Y_j = 1$. However, this approach would accumulate numerical errors of all $N - 1$ species to the Nth specie. This is numerically acceptable provided the Nth species maintains a sufficiently high mass fraction (> 0.5) throughout the computational domain, a condition satisfied in the HM2 test case presented in this paper.

3.1.3. Momentum conservation equation

$$\frac{\partial \rho \vec{U}}{\partial t} + \nabla \cdot \left(\rho \vec{U} \otimes \vec{U}\right) = -\nabla p + \nabla \cdot \tau + \rho \vec{g} + \vec{S}_u \tag{3}$$

where p is the pressure and $\vec{S}_u$ represents the momentum sink term due to condensation. The $\rho \vec{g}$ term addresses the buoyancy effects, where $\vec{g}$ is the gravitational vector. The shear stress tensor accounts both viscous and turbulent stresses and is defined as:

$$\tau = \rho \left(\nu + \nu_t\right) \left[\nabla \vec{U} + \left(\nabla \vec{U}\right)^T - \frac{2}{3} \delta \nabla \cdot \vec{U}\right] \tag{4}$$

where ν denotes the gas mixture kinematic viscosity, ν_t represents the turbulent eddy viscosity obtained turbulence model and δ is the Kronecker delta.

3.1.4. Energy conservation equation

The energy conservation equation is defined in terms the gas mixture enthalpy h:

$$\frac{\partial \rho h}{\partial t} + \nabla \cdot \left(\rho \vec{U} h\right) + \frac{\partial \rho K}{\partial t} + \nabla \cdot \left(\rho \vec{U} K\right) = \rho \vec{U} \cdot \vec{g} + \frac{\partial p}{\partial t} + \nabla \cdot \left[\left(\lambda + \frac{C_p \nu_t}{Pr_t}\right) \nabla T\right] + \sum_j \nabla \cdot \left[\rho h_j \left(D_{j,m} + D_t\right) \nabla Y_j\right] + S_h \tag{5}$$

where $K = 1/2|\vec{U}|^2$ denotes the specific kinetic energy. On the RHS, the first term accounts for the work done by gravitational force, second term addresses pressure work. The third term corresponds to the enthalpy flux due to conduction (both laminar and turbulent contributions), where λ denotes the molecular thermal conductivity, C_p represents the specific heat capacity, and T denotes the temperature of the gas mixture. The fourth term covers the enthalpy transport resulting from the diffusive transport of the species. The last term S_h accounts for the sink term arising from condensation.

3.1.5. Ideal gas state equation

The gas mixture is generally considered to be an ideal gas in containment applications and based on that assumption; the gas mixture density is given by:

$$\rho = \frac{pW}{RT} \tag{6}$$

where $W = \left(\sum_{k=1}^{N} Y_k / W_k\right)^{-1}$ represents the molar mass of the gas mixture calculated by mass fraction weighted harmonic averaging of species molar mass. Here W_k is the molar mass of the kth species and R is the universal gas constant. While steam near saturation conditions deviates slightly from ideal gas behavior, at HM2 test conditions (1.2 bar $< p <$ 1.5 bar, 20 °C $< T <$ 105 °C), this results in $<$ 2% error in mixture density predictions, which is acceptable for the current application.

3.1.6. Turbulence transport equations

The standard $k-\omega$ SST turbulence model transport equations (Menter et al., 2003b) with additional buoyancy related terms (Kampili et al., 2021) is given by:

$$\frac{\partial(\rho k)}{\partial t} + \nabla \cdot (\rho \vec{U} k) = \nabla \cdot [(\mu + \sigma_k \mu_t) \nabla k] + P_k + P_{k,b} - \beta^* \omega k + S_k \tag{7}$$

$$\frac{\partial(\rho \omega)}{\partial t} + \nabla \cdot (\rho \vec{U} \omega) = \nabla \cdot [(\mu + \sigma_\omega \mu_t) \nabla \omega] + 2(1 - F_1) \frac{\rho \sigma_{\omega 2}}{\omega} \nabla k \cdot \nabla \omega + \frac{\gamma}{\nu_t} P_k + P_{\omega,b} - \beta \rho \omega^2 + S_\omega \tag{8}$$

where the eddy viscosity μ_t is given by

$$\mu_t = \frac{\rho a_1 k}{\max\left(a_1 \omega, S F_2\right)} \tag{9}$$

and ν_t is the turbulent kinematic viscosity. P_k represents the turbulence production term given by

$$P_k = \min\left(\tau \nabla \vec{U}_g, 10 \beta^* k \omega\right) \tag{10}$$

The term $P_{k,b}$ represents turbulence production due to buoyancy, while $P_{\omega,b}$ denotes turbulence dissipation caused by buoyancy; both terms are formulated using the Simple Gradient Diffusion Hypothesis (SGDH) approach (Chung and Devaud, 2008).

$$P_{k,b} = \frac{\mu_t}{\sigma_t} \tag{11}$$

$$P_{\omega,b} = \frac{\rho}{\mu_t} \left[\left(\gamma_1 + 1\right)\left(1 - C_{3\omega}\right) \cdot \max\left(P_{k,b}, 0\right) - P_{k,b}\right] \tag{12}$$

where β^*, σ_k, σ_t, β, σ_ω, $\sigma_{\omega 2}$, γ_1, $C_{3\omega}$ and a_1 are model constants, F_1 and F_2 are blending functions, and S denotes the strain invariant; all of these are defined and calculated in accordance with the standard $k-\omega$ SST turbulence model. The S_k and S_ω terms account for the sink terms due to condensation.

3.1.7. Fog droplet transport equations

The fog droplets generated through bulk condensation are transported using a Eulerian passive scalar approach. In this passive method (one-way coupling), the influence of droplets on the carrier gas properties and flow physics is neglected, yet they can move relative to the primary flow field. These droplets become suspended within the gas mixture are transported by the gas velocity field, turbulent diffusion and drift velocity. The drift velocity accounts for the relative motion of the droplets with respect to the gas flow field, driven by gravity, drag and inertial forces. For droplet volume fractions between 0.0001% and 0.1%, the one-way coupling approach may become insufficient, as the momentum transfer from the droplet due to relative motion can alter the gas flow turbulent structure (Elghobashi, 1994). Two-way coupling would be required to capture such effects; however, it is neglected in the present work for simplicity and remains a topic for future investigation. The diffusion by Brownian motion is disregarded in the present work due to its lower contribution compared to turbulent diffusion. Moreover, the droplet-droplet interactions are considered negligible, an assumption valid for fog volume fractions below 0.1% (Elghobashi, 1994), which typically applies to most containment scenarios. Consequently, the fog transport equation (George et al., 2023) is expressed in terms of fog volume fraction (α_f).

$$\frac{\partial\left(\rho_f \alpha_f\right)}{\partial t} + \nabla \cdot \left[\rho_f \left(\vec{U} + \vec{U}_d\right) \alpha_f\right] = \nabla \cdot \left(\rho_f D_t \nabla \alpha_f\right) + S_{m,f} \tag{13}$$

where ρ_f is the density of the fog material (water = 1000 kg/m^3) and $S_{m,f}$ corresponds to the source term due to condensation, which equal and opposite to the source term (S_m)in the gas total mass conservation equation (Eq. (1)). The drift velocity is determined by solving the force balance equation (Manninen et al., 1996; Frederix et al., 2017) of a droplet, which can be further simplified by assuming that the droplet acceleration is equal to the instantaneous acceleration of the local gas flow. Consequently, the drift velocity relation is given by:

$$\vec{U}_d = \left(\frac{\rho_f - \rho}{\rho_f}\right) \frac{\tau_f}{C_d} \vec{g} - \frac{\tau_f}{C_d} \frac{\partial \vec{U}}{\partial t} \tag{14}$$

where $\tau_f = \frac{\rho_f d_f^2}{18\mu}$ is the droplet relaxation time, which is a function of the droplet diameter (d_f). The drag coefficient (C_d) is determined using Schiller–Naumann relation (Schiller and Naumann, 1935). The drag coefficient is function of the drift velocity and is calculated using the $\vec{U}_d$ from the previous iteration. This simplified approach is justified because local drift velocity variations between time steps are small – dominated by gravity – and can converge within the PIMPLE iterations.

3.1.8. Conjugate heat transfer

The containment internal solid structures and outer walls have significant thermal inertia, can function as heat sinks or sources depending on the surrounding temperature, and consequently interact with the containment atmosphere. Furthermore, the latent heat released during wall condensation is transferred onto these solids, as a heat flux at the solid–fluid interface. Consequently, a conjugate heat transfer analysis (CHT) is essential to model the coupled behavior of solid and fluid phenomena within the solid region and at the solid–fluid interface. The heat transfer within the solid region is governed by Fourier's law of heat conduction given by:

$$\rho_s C_{p,s} \frac{\partial T_s}{\partial t} = \lambda_s \nabla^2 T_s \tag{15}$$

where ρ_s is the solid material density, T_s represents the solid temperature field, $C_{p,s}$ denotes the solid's specific heat capacity and λ_s is the thermal conductivity of the solid. The heat transfer at the interface is coupled by using a temperature boundary condition, which is solved to obtain the interface temperature (T_i):

$$q''_{c,i} + \lambda_{f,eff,i}\frac{T_{c,f} - T_i}{\delta_{c,f-i}} = \lambda_s \frac{T_i - T_{c,s}}{\delta_{c,s-i}} \tag{16}$$

where $q''_{c,i}$ quantifies the heat flux at the interface due to wall condensation. Here, $\lambda_{f,eff,i} = \lambda + \frac{C_p \nu_t}{Pr_t}$ is the effective (laminar and turbulent) thermal conductivity of the gas mixture, while λ_s refers to the thermal conductivity of the solid, both at the interface. The temperatures $T_{c,f}$ and $T_{c,s}$ correspond to the near wall cell center temperatures of the fluid and solid region, respectively. Likewise, the distances $\delta_{c,f-i}$ and $\delta_{c,s-i}$ represents the distance between the cell center and interface for fluid and solid regions, respectively.

3.2. Condensation modeling

3.2.1. Wall condensation modeling

The wall condensation model in *containmentFOAM* uses diffusion layer method combined with face-flux approach (Vijaya Kumar et al., 2021) to compute the condensation mass flux at the wall boundaries. Unlike conventional methods that apply a volumetric sink term in the near-wall cell for condensation and enforce a no-slip condition at the wall (Dehbi et al., 2013), the face-flux approach introduces a suction velocity normal to the wall. This velocity is defined such that its associated mass flux matches the computed condensation flux, effectively removing the condensed mass directly through the wall boundary. This suction velocity takes care of the sink terms due to condensation in all conservation equations via the convection term. The liquid volume formed during wall condensation is not modeled in the present work, as accumulated volume remains negligible relative to the gas phase during the HM2 transient. The condensed liquid film drains to the vessel sump, and the accumulated water accounts for less than 5% of the vessel volume, thereby having negligible effect on vessel pressure evolution during the short transient duration of the HM2 test. Moreover, the vessel walls remain sufficiently cold throughout the entire transient to preclude significant re-evaporation of condensed films. However, during extended transients with longer timescales, accumulated liquid can become significant and may re-evaporate, potentially affecting long-term containment conditions. This requires explicit modeling of liquid film flow and accumulation using approaches such as thin-film or Volume of Fluid (VOF) methods, which remain topics for future investigation. For the HM2 test case, the present wall condensation model is therefore appropriate, and the condensation mass flux is given by:

$$\dot{m}''_{wall} = \frac{\rho D_{H_2O,m,face}}{1 - Y_{H_2O,sat,face}} \frac{Y_{H_2O,cell} - Y_{H_2O,sat,face}}{\delta_{cell-face}} \tag{17}$$

where $D_{H_2O,m,face}$ denotes the effective diffusivity (molecular and turbulent) of steam in the gas. The wall steam mass fraction is enforced to be equal to saturated steam mass fraction ($Y_{H_2O,sat,face}$) using a boundary condition and the gradient of the steam mass fraction (Y_{H_2O}) is the driving force for wall condensation. This gradient is calculated using cell center steam mass fraction ($Y_{H_2O,cell}$) and distance between the cell center and wall face ($\delta_{cell-face}$). The corresponding suction velocity normal to the wall ($\vec{n}_{wall}$) is computed as:

$$\vec{U}_{wall} = \frac{\dot{m}''_{wall}}{\rho}\vec{n}_{wall} \tag{18}$$

The face-flux approach offers notable advantages over the volumetric source or sink approach, demonstrating improved convergence behavior, mass conservation and grid-independence as well as the elimination of any need for suction-related correction factors (Vijaya Kumar et al., 2021). The latent heat released during wall condensation is incorporated as a heat flux ($q''_{c,i}$) at the solid–fluid interface into the interface boundary condition (Eq. (16)).

$$q''_{c,i} = \dot{m}''_{wall} h_{lg} \tag{19}$$

3.2.2. Bulk condensation modeling

The present work employs two distinct bulk condensation models—the saturation temperature equilibrium model and the classical nucleation model, to assess how the choice of bulk condensation modeling influences simulation results.

Saturation temperature equilibrium (STE) model

The saturation temperature equilibrium (STE) model is based on the "return to saturation at constant timescale" method by Vyskocil et al. (2014) and has been previously implemented and validated within *containmentFOAM* (George et al., 2023). This model operates by maintaining the local mixture at saturation temperature by condensing the surplus steam or by evaporating the excess fog, within each simulation time step (Δt). The latent heat (h_{lg}) released during condensation or absorbed during evaporation facilitates bringing the local mixture to saturation temperature. Consequently, the volumetric bulk condensation rate is given by:

$$\dot{m}'''_{bulk} = \frac{\dot{Q}'''}{h_{lg}} \tag{20}$$

where the driving thermal energy, $\dot{Q}'''$ is expressed as:

$$\dot{Q}''' = \rho C_p \frac{T_{sat} - T}{\Delta t} \tag{21}$$

where T_{sat} denotes the saturation temperature determined from the steam partial pressure, using the Antoine relation (Antoine, 1888; Perry et al., 2018). Furthermore, the $\dot{Q}'''$ is constrained by the local availability of steam and fog to avoid unphysical values. The fog transport equation, when combined with the STE model, utilizes monodispersed droplet size that is defined based on previous studies (Zhang and Laurien, 2014; George et al., 2023).

Classical nucleation theory (CNT) model

The classical nucleation theory (CNT) model used in this study follows the framework presented by Sidorov and Yastrebov (2023), which is based on Frenkel-Zel'dovich classical nucleation theory. This model accounts for the nucleation, growth and transport of droplets generated during bulk condensation by employing a kinetic equation module and the method of moments. Bulk condensation is triggered when the local steam partial pressure (p_{H_2O}) exceeds the saturation pressure (p_{sat}) at the local temperature. This is quantified by the degree of supersaturation ($s = p_{H_2O}/p_{sat}(T)$), which must be greater than unity to initiate nucleation. Only droplets exceeding a certain critical radius are stable and capable of growing in supersaturated steam environments, and this critical radius (r_{cr}) is computed using Thompson formula:

$$r_{cr} = \frac{2\sigma W_{H_2O}}{\rho_f RT \ln s} \tag{22}$$

where σ is the surface tension and W_{H_2O} represents the molar mass of steam. Subsequently, the number of droplets with critical radius generated per unit volume, known as nucleation rate (I) is given by:

$$I = \left(\frac{\beta}{\rho_f}\right)\left(\frac{p_{H_2O}}{RT}\right)^2 \sqrt{\frac{2W_{H_2O}\sigma N_A^3}{\pi}} \times \exp\left[-\frac{16\pi N_A \left(\frac{\sigma}{R}\right)^3 \left(\frac{W_{H_2O}}{\rho_f}\right)^2}{3T^3(\ln s)^2}\right] \tag{23}$$

N_A denotes the Avogadro number, and β is the condensation coefficient ranging between 0 and 1. For the simulations in the present work, $\beta = 0.1$ was determined through sensitivity studies showing numerical

Table 1
Source terms for mass, species, momentum, energy, turbulence and fog transport equations.

Conservation equation	Source/sink term
Total mass	$S_m = -\dot{m}'''_{bulk}$
Species mass	$S_j = \begin{cases} S_m & \text{if } j = \mathrm{H_2O} \\ 0 & \text{if } j \neq \mathrm{H_2O} \end{cases}$
Momentum	$\vec{S}_U = S_m \vec{U}$
Energy	$S_h = S_m C_{p,\mathrm{H_2O}} T - S_m h_{lg}$
Turbulent kinetic energy	$S_k = S_m k$
Turbulent dissipation rate	$S_\omega = S_m \omega$
Fog transport	$S_{m,f} = \dot{m}'''_{bulk}$

$C_{p,H_2O} = f(p,T)$ is a function of local gas pressure and temperature.

instability (oscillations and divergence) for $\beta > 0.2$ due to over-prediction of condensation rates at the simulation time-step sizes. Next, the nucleated droplets grow by further condensation on their surfaces, with the droplet growth rate governed by the Hertz–Knudsen equation:

$$\dot{r} = \frac{dr}{dt} = \beta \frac{p_{sat}}{\rho_f} \left(\frac{(s-1)\sqrt{W_{\mathrm{H_2O}}}}{\sqrt{2\pi RT}} \right) \tag{24}$$

The droplet size distribution function is governed by a kinetic equation that accounts for the nucleation and growth, from which the system of moment equations is derived. This approach does not directly use the droplet size distribution function but instead relies on first four moments – number density (number of droplets per unit volume), mean radius (per unit volume), mean surface area (per unit volume) and volume (per unit volume) – capturing the essential features of the droplet. The final system of moment equations is adapted to the CFD framework by expressing them as passive scalar transport equation based on Eq. (13):

$$\frac{\partial \left(\rho_f M_n\right)}{\partial t} + \nabla \cdot \left[\rho_f \left(\vec{U} + \vec{U}_d \right) M_n \right] = \nabla \cdot \left(\rho_f D_t \nabla M_n \right) + S_{M_n} \tag{25}$$

where $n = \{0, 1, 2, 3\}$ corresponds to the first four moments M_0, M_1, M_2 and M_3, and the drift velocity calculated using Eq. (14) as a function of mean droplet diameter $d_{mean} = 2M_1/M_0$. Subsequently, the source terms in the moment equation are defined as:

$$\left.\begin{aligned} S_{M_0} &= I\rho_f; \\ S_{M_1} &= I\rho_f r_{cr} + \dot{r}\rho_f M_0; \\ S_{M_2} &= I\rho_f r_{cr}^2 + 2\dot{r}\rho_f M_1; \\ S_{M_3} &= I\rho_f r_{cr}^3 + 3\dot{r}\rho_f M_2; \end{aligned}\right\} \tag{26}$$

Moreover, the evolution of droplet size resulting from coalescence or breakup of droplets is neglected for simplicity in this study. Finally, the net volumetric bulk condensation rate can be determined from the nucleation rate, growth rate and moment values as follows:

$$\dot{m}'''_{bulk} = \frac{4}{3}\pi r_{cr}^3 \rho_f I + 4\pi\rho_f \dot{r} M_2 \tag{27}$$

The verification of this CNT bulk condensation model was conducted using the Mollier mixing nozzle test case, following the procedure detailed in George et al. (2023). The model predictions for condensation rate, final temperature and fog content were found to be within 90% accuracy. However, these verification details are omitted in this paper for the sake of brevity.

Bulk condensation source terms

The bulk condensation results in volumetric source terms in the conservation equations, which is summarized in Table 1.

4. Simulation setup

4.1. Test phenomenology

To establish the basis for the subsequent simulation setup, the phenomenology of the experiment in phases 2 and 3 is first described, since the evolving flow and mixing characteristics are critical for interpreting the experimental data and corresponding simulations. The overall flow development and steam transport inside the vessel are best illustrated using snapshots from CNT HM2 simulation showing the combined velocity vector fields and steam concentration distributions at different times during the test (Fig. 2). These simulation visualizations highlight the temporal sequence of events, from the initial steam release to the final homogenization of the vessel atmosphere, demonstrating the processes driving mixing and cloud erosion. The times shown in the snapshots and discussed below correspond to simulation times where key phenomena closely match the experimental observation, with $t = 0$ defined as the start of steam injection in both cases.

At the onset of steam injection (t = 0–100 s), the jet emerging into the inner cylinder rapidly displaces the pre-existing hydrogen-rich gas. The injected steam plume effectively mixes the hydrogen and nitrogen within the cylinder, reducing its concentration. The injected steam undergoes condensation both in the bulk and on the cold walls of the inner cylinder as it ascends. Subsequently (t = 300–700 s), the mixture overflows the upper edge of the inner cylinder into the annular region, where further dilution of hydrogen occurs, while the steam mixture plume progresses downward within this annular space. Simultaneously, the steam plume ascends towards the vessel dome. During this interval, steam interacts with the vessel walls, promoting wall condensation on these cold surfaces. As the steam plume in the annular region reaches and enters the lower edge of the inner cylinder, a natural convection loop is gradually established between the inner cylinder and the annulus.

As the injection continues ($t \approx 1200$ s), steam jet progresses towards the dome, leading to the gradual mixing and erosion of the hydrogen cloud. When the steam plume contacts the cold dome ($t \approx 1500$ s), there is a sudden increase in the wall condensation rate accompanied by a drop in vessel pressure. Consequently, a larger convection loop develops between the inner cylinder and the annular region, extending from the injection zone up to the dome. The velocity vector fields highlight the dominant upward jet in the inner cylinder and the resulting recirculating flow in the annulus, while the steam concentration contours track the gradual erosion of the hydrogen-rich cloud in the dome. The large convection loop homogenizes the vessel atmosphere and dissolves the hydrogen cloud until the end of steam injection ($t \approx$ 2500 s). Subsequently, the flow gradually stagnates ($t \approx$ 3000 s), with residual motions, primarily in the upper regions due to gradual buoyant rise of previously injected steam.

4.2. Computational domain and mesh

The computation domain, shown in Fig. 1, is simplified to one-fourth of the full domain due to its symmetric nature. The domain is divided into three regions based on their properties and flow characteristics: one, the fluid region containing multi-component gas mixture; two, the solid region, which includes the inner cylinder, condensate trays, vessel inner and outer walls, all made of stainless steel; third, coolant region modeled as a solid region with thermal oil properties since the oil is stagnant during the experiment, leading to heat transfer predominantly by conduction. Moreover, the simulations using only the fluid region are challenging due to limited experimental data availability at the boundaries, making it difficult to apply appropriate boundary conditions. The steam injection nozzle is represented in the fluid region as a cylinder with an inlet positioned on its top surface. Furthermore, since the hydrogen injection phase is not simulated, the hydrogen nozzle is omitted from the computational domain. Following this, a block structured hexahedra mesh (Fig. 3) is generated using ICEM-CFD software, following the best practice guidelines (BPG) (Nuclear Energy Agency (NEA), OECD, 2025).

The above mesh is selected based on the grid sensitivity study, which will be discussed in Section 4.4. The mesh consists of approximately 0.5 million elements, with, 0.4 million in the fluid region, 75,000 in the solid region and 15,000 in the coolant region. In the fluid mesh, near wall cells are resolved to achieve a $y^+ \approx 1$ to accurately capture the boundary phenomena, especially wall condensation rates.

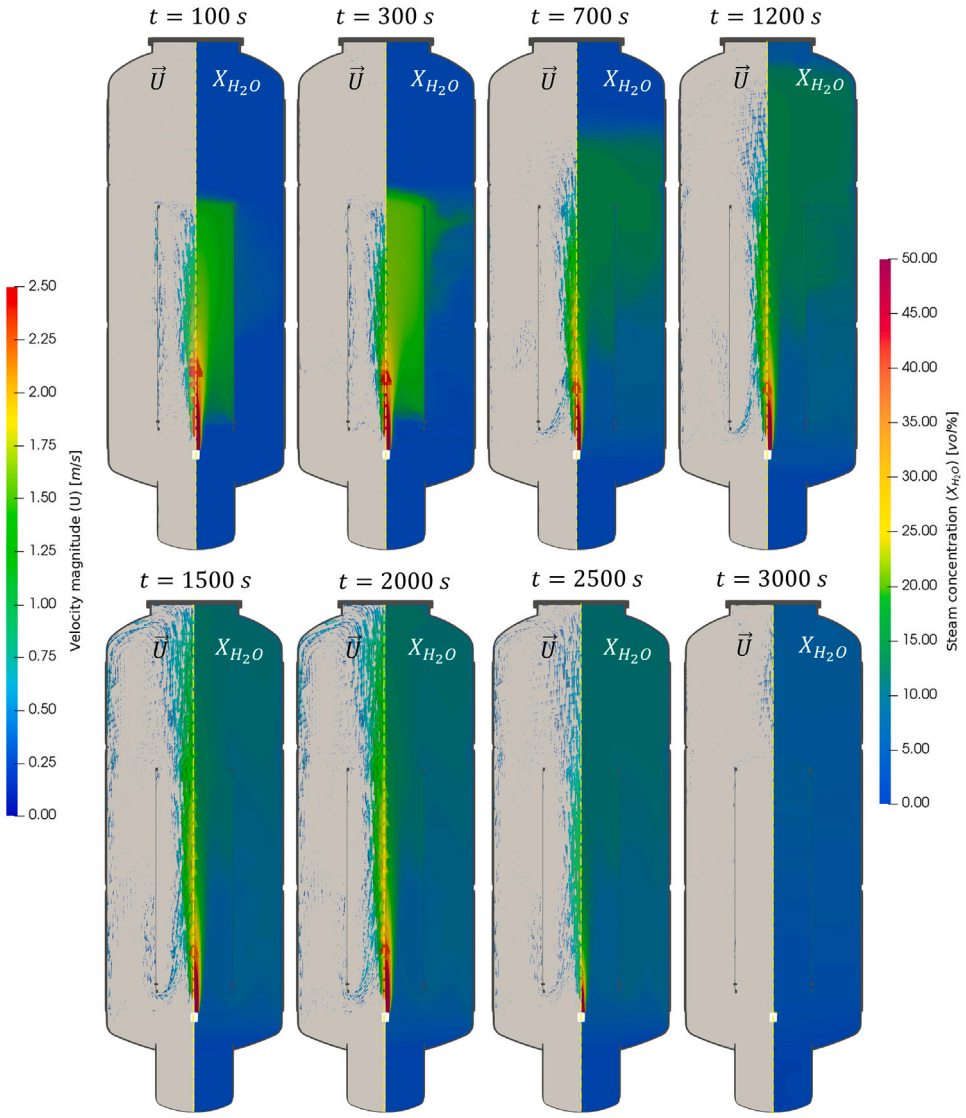

Fig. 2. Phenomenological representation (snapshots from CNT HM2 simulation) of the HM2 test: velocity vector fields ($\vec{U}$, left section of each image) and steam concentration contours (X_{H_2O}, right section of each image), illustrating the temporal evolution of flow and mixing during the experiment.

4.3. Initial and boundary conditions

Since the numerical simulations cover only the durations of phase 2 (steam injection) and phase 3 (no injection), the computation domain is initialized with experimental data from the beginning of phase 2. The initial fluid is assumed to be stagnant, and the vessel is pressurized to 1.259 bar. The initial distributions of fluid temperature and hydrogen concentration (shown in Fig. 4) are generated by linearly interpolating the sensor measurements of gas temperature and hydrogen concentration along the vertical axis of the vessel, while neglecting any circumferential variations. A similar interpolation approach is employed for the solid and coolant regions to initialize their temperatures, using wall temperature sensor data. This ensures that the readings at the measurement locations (Fig. 1) are consistent between the experiment and the simulation's initial conditions, as confirmed by the vertical profiles in Fig. 4. The remaining gaseous region, after hydrogen is accounted for, consists of nitrogen (97%), steam (2%), and oxygen (1%), consistent with the experimental gas composition.

The boundary conditions for the THAI HM2 simulations are summarized in Table 2. During the steam injection phase, the mass flow rate is around 24 g/s, which is then reduced to zero in phase 3. However, there are minor variations in the experimental mass flow rates with time. In order to account for that and ensure mass consistency in both experiment and simulation, a time-dependent mass flow rate is specified at the injection boundary. A similar approach is adopted for the injection temperature, which is maintained at around 105 °C during phase 2, but is also prescribed as a time-dependent boundary condition to capture variations observed in the experiment. As only steam is supplied at the injection boundary, the mass fraction of steam is set to 1.0, while the mass fractions of all non-condensable gases (N_2, H_2 and O_2) are specified as zero. A turbulence intensity of 5% is used to estimate the turbulent kinetic energy and eddy frequency at the injection boundary. The specific dissipation rate at the injection boundary is estimated based on a specified mixing length (3% of nozzle diameter) and local velocity field. The temperature boundary condition vessel walls in the fluid region uses a conjugate heat transfer (CHT) boundary condition (Eq. (16)) as it is coupled with the inner walls in the solid region. On these fluid region walls, the steam mass fraction is specified using a saturated steam mass fraction boundary condition, while the non-condensable gases are assigned a non-condensable mass fraction boundary condition to compensate for the convective flux through an opposing diffusive flux (Vijaya Kumar et al., 2021). Furthermore, these walls are assigned a zero gradient boundary condition

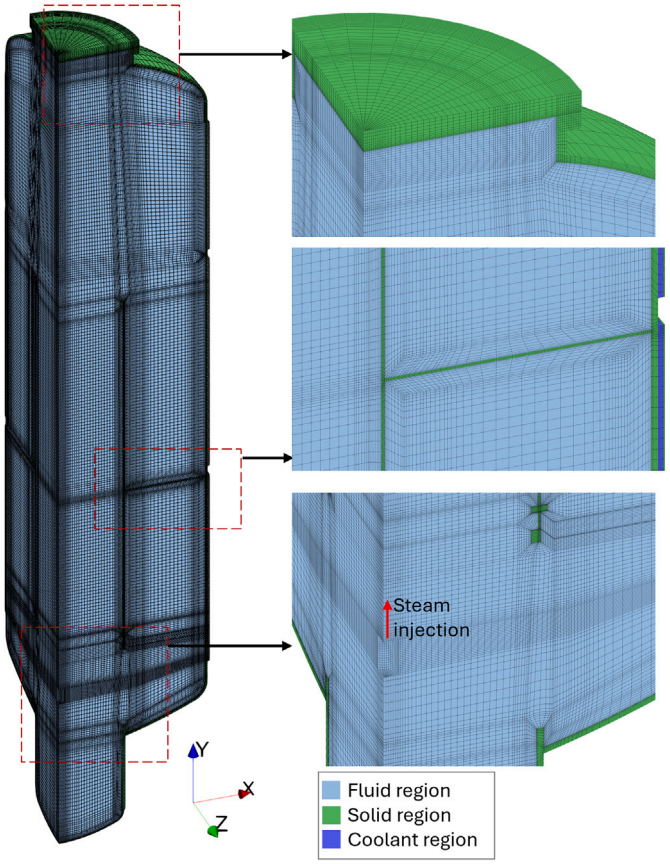

Fig. 3. Quarter-symmetric structured HM2 mesh comprising fluid, solid and coolant regions.

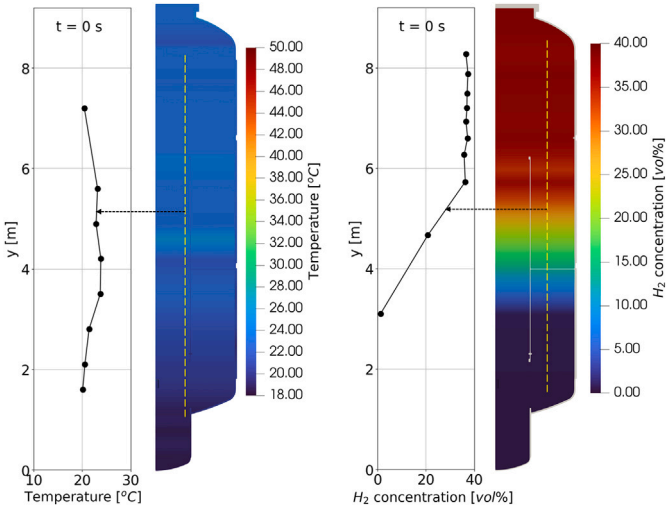

Fig. 4. Initial simulation temperature and hydrogen distributions, interpolated from HM2 experimental sensor data at the start of phase 2.

for turbulent kinetic energy, while a wall function is used to estimate the values for eddy frequency (Menter et al., 2003a). The heat transfer by means of radiation is neglected as preliminary HM2 short transient studies using Monte Carlo method (Liu et al., 2022) showed minor improvements relative to bulk condensation effects while incurring excessive computational cost.

In the present analysis, the oil coolant is treated as a solid medium that functions as a heat sink, i.e., it only absorbs thermal energy without convective transport. For the walls in both solid and coolant regions, a CHT boundary condition is used for temperature to couple the heat transfer between adjacent regions. For the vessel outer wall in the solid region, outside of which is the rockwool thermal insulation, a convective heat transfer coefficient boundary condition is used. The heat transfer coefficient ($h \approx 0.5$) at the boundary wall is calculated by considering the thermal insulation thickness and its thermal conductivity, in addition to the natural convection heat transfer coefficient. The ambient temperature for the convective heat transfer coefficient boundary condition is set to 25 °C, obtained from experimental data. For all symmetric walls in the fluid, solid and coolant regions, a symmetric boundary condition is applied for all fields to ensure that there is no net flux across these planes and normal components of all fields are zero.

4.4. Grid sensitivity study

A systematic grid sensitivity study is conducted using three different mesh-resolutions-coarse, medium and fine, to ensure mesh independence on the results. Each finer mesh is generated by refining the preceding mesh uniformly by a factor of two in all spatial directions. The Grid Convergence Index (GCI) methodology (Celik and Zhang, 1995) is applied to evaluate the solution convergence with respect to the mesh. The key parameters used for GCI analysis include, the jet velocity profile, hydrogen concentration, integral wall heat flux, integral wall condensation rate and integral bulk condensation rate. The jet velocity profile, which characterizes the momentum and mixing intensity, is extracted at 0.2 m above the injection nozzle. The hydrogen concentration, providing insight into stratification erosion, is measured at height of 5 m from the vessel base. The integral wall heat flux and wall condensation rates, measured at the vessel walls, reflect how boundary layer resolution influences heat transfer and wall condensation. Lastly, the integral bulk condensation rate indicates how the overall mesh resolution affects the total bulk condensation rate. The grid sensitivity simulations are performed using the CNT bulk condensation model. The findings from the GCI analysis is summarized in Table 3. The GCI values for all parameters are below 3% on the medium mesh and below 1% on the fine mesh, indicating acceptable grid convergence.

From the computational efficiency perspective, the coarse mesh required 1.3 h of clock time for 100 s transient simulation, the medium mesh about 27 h and the fine mesh about 115 h, highlighting the substantial increase in computational cost with mesh refinement. Consequently, the grid sensitivity simulations are limited to a duration of 100 s, sufficient to capture initial transient behavior inside the vessel. Based on the grid sensitivity results, the medium mesh is selected for the final HM2 simulations, offering good compromise between numerical accuracy and computational efficiency.

4.5. Numerical schemes and solution methods

The *containmentFOAM* solver employs the numerical schemes and solution methods provided by OpenFOAM (OpenFOAM, 2023). Second-order accurate spatial and temporal discretization, which are suitable for high-quality structured meshes, are utilized to ensure a good balance between numerical accuracy and computational efficiency. The temporal discretization uses a weighted blending between the implicit Euler and Crank–Nicolson schemes, controlled with a blending factor (ψ) of 0.9. In OpenFOAM, this corresponds to $\theta = \frac{1}{1+\psi} = 0.526$, where $\theta = 0.5$ represents Crank–Nicolson scheme and $\theta = 1$ represents fully implicit Euler. For spatial discretization, the convection terms use Gauss liner upwind scheme, gradient terms are handled using Gauss linear scheme and Laplacian terms utilize Gauss linear scheme with non-orthogonal corrections.

Table 2
Boundary conditions for HM2 simulation setup.

(a) Fluid Region

Boundary	T	p	U	Y_{H_2O}	Y^*_{nc}	k	ω
Injection	Experiment ($\approx 105\,^oC$)	Zero gradient	Calculated from mass flow rate	1.0	0.0	5% intensity	Fixed value
Injection wall	Adiabatic	Zero gradient	No slip	Zero gradient	Zero gradient	Zero gradient	Wall function
Vessel walls	CHT	Zero gradient	No slip	Saturated steam mass fraction	Non-condensable mass fraction	Zero gradient	Wall function
Symmetric walls	Symmetry	Symmetry	Symmetry	Symmetry	Symmetry	Symmetry	Symmetry

$^*nc = \{H_2, O_2, N_2\}$

(b) Solid Region

Boundary	T
Inner walls	CHT
Coolant walls	CHT
Outer wall	Convective heat transfer coefficient
Symmetric walls	Symmetry

(c) Coolant Region

Boundary	T
Vessel inner wall	CHT
Vessel outer wall	CHT
Symmetric walls	Symmetry

Table 3
Grid sensitivity study results of HM2.

Parameter	Coarse	Medium	Fine
Number of elements	71,088	568,704	4,549,632
Centerline jet velocity (m/s)	2.592	2.662	2.669
GCI - centerline jet velocity (%)		0.365	0.036
Hydrogen concentration ($vol\%$)	4.344	4.972	5.377
GCI - hydrogen concentration (%)		6.096	1.118
Integral wall heat flux (kW)	−9.812	−9.826	−9.831
GCI - integral wall heat flux (%)		0.053	0.012
Integral wall condensation rate (g/s)	3.557	3.572	3.581
GCI - integral wall condensation rate (%)		0.274	0.079
Integral bulk condensation rate (g/s)	0.135	0.140	0.141
GCI - integral bulk condensation rate (%)		2.232	0.835

The solution method uses a segregated approach, where the conservation equations are solved sequentially rather than simultaneously. The multi-region equations are solved by making use of the modular solver framework available since OpenFOAM-11 version. The coupling between pressure and velocity fields utilizes the PIMPLE algorithm. All the discretized equations are solved using the stabilized preconditioned biconjugate gradient (PBiCGStab) method, except for pressure equation, which utilizes preconditioned conjugate gradient (PCG) method. The convergence criteria consist of a tolerance of 10^{-6} for the iterative solvers of the discretized equations and a global tolerance of 10^{-4} for convergence within each time step. The time-step size estimated utilizing adaptive time-stepping method based on Courant–Friedrichs–Lewy (CFL) constraints. A maximum Courant number of 0.8 is used throughout the simulations to ensure stability and accuracy of the simulations.

5. Results and discussion

5.1. Validation strategy

The validation of the simulation results focuses on replicating key phenomena observed experimentally in the THAI HM2 test. This involves detailed comparison of temperature and hydrogen concentration profiles, as well as vessel pressure evolution, between the simulation and experimental measurements. The hydrogen and temperature fields are examined along the vessel height at regular time intervals to evaluate the important phenomena like hydrogen cloud dissolution, steam jet penetration and overall gas mixing dynamics. The transient vessel pressure serves as an indirect indicator of the impact of both wall and bulk condensation since direct experimental measurements of their rates are not available. These quantities are essential for assessing and drawing conclusions about the influence of bulk condensation on buoyancy-driven flows within containment.

Beyond these primary metrics, the investigations extend to analyze how variations in density and resultant velocities driven by buoyancy forces evolve spatially and temporally, offering deeper insight into the mechanism driving the flow acceleration and cloud erosion. The relative contributions of wall and bulk condensation to the integral condensation rates are examined to understand how different modeling approaches affect the interactions. Particular attention is given to the source terms due to local latent heat release and establish its influence on thermal and dynamic events inside the vessel. The distribution of the fog droplets is also analyzed to understand the transport of the droplets, which may play a significant role in scenarios where fog re-evaporation causes relative cooling of the surrounding gas mixture.

As the primary objective of this work is to evaluate the impact of bulk condensation model on the containment atmosphere, the simulations are conducted with and without the bulk condensation model activated. The baseline simulation accounts only wall condensation model together with other relevant phenomena, while main cases incorporate bulk condensation model into it. Moreover, two bulk condensation models, namely saturation temperature equilibrium (STE) model and classical nucleation theory (CNT) model, are employed to assess the influence of the bulk condensation modeling approaches. For the STE model, a constant fog droplet diameter of 20 μm was deliberately selected to highlight the effect of results to arbitrary diameter choice against the physically predicted droplet evolution from the CNT approach.

In the following sections, the labels “WCM” and “BWCM” are used to identify different simulation approaches: “WCM” denotes baseline simulations using only the wall condensation model, while “BWCM” refers to simulations that incorporate both bulk and wall condensation models. To further distinguish between the two bulk condensation

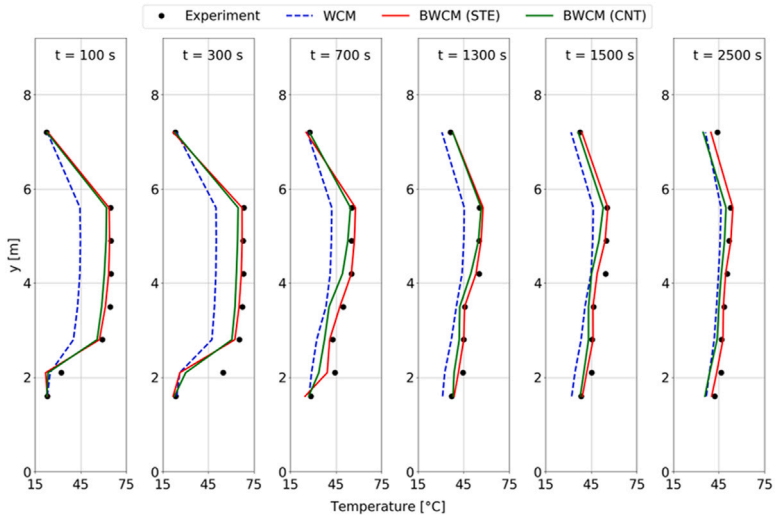

Fig. 5. Comparison of experimental and simulated gas temperature evolution along the vessel height within the inner cylinder region.

models, simulations utilizing the saturation temperature equilibrium approach are labeled "(STE)", whereas those applying the classical nucleation theory model are labeled "(CNT)".

5.2. Temperature profile evolution and latent heat source distribution

The temporal evolution of the vertical temperature profile within the inner cylinder region is shown in Fig. 5. At all time points, simulations incorporating bulk condensation model consistently predict higher temperatures than the baseline simulation and closely match the experimental measurements at various vessel heights. The baseline simulation shows deviations of around 15 to 20 °C during the initial stages (t = 100–400 s), which decrease to approximately 5–10 °C in the mid-stages (t = 700–1300 s), and further reduce to roughly 2–5 °C during the final stages (t = 1500–2500 s). However, the simulations with bulk condensation model exhibit only minor differences of around 2–5 °C during the initial stages, except at location very close to the injection nozzle, and even smaller ($\approx$ 1 °C) during the mid and final stages. Hence, the bulk condensation models demonstrate excellent overall agreement with the experimental observations throughout the transient. Moreover, both condensation models- the STE and CNT approaches-yield similar temperature predictions inside the vessel and consistently outperform the wall condensation-only simulation in matching the measured data.

The improved agreement is primarily attributed to the localized release of latent heat associated with bulk condensation in the inner cylinder region downstream of the injector, which acts as a significant heat source and raises the local gas temperatures. This effect is absent in the baseline simulation, where only wall condensation is considered, resulting in an underprediction of the measured temperatures. The presence and impact of this latent heat release is further confirmed by the sectional distribution of temperature and energy source term (Fig. 6) at t = 300 s, clearly illustrating the higher temperatures and the heat sources in the bulk condensing region. The BWCM simulations exhibit a deeper penetration of the steam plume into the hydrogen layer. As a result, some hot steam escapes through the upper opening of the inner cylinder, mixing with the surrounding gases and subsequently flowing downward within the annular gap. A similar process will occur in the WCM case, but at a later time due to the slower development of the steam plume's interaction with the hydrogen layer.

The spatial distribution of the latent heat source shows notable differences, which is linked specifically to their respective modeling approaches. The STE model instantaneously drives the local mixture to its saturation temperature, causing bulk condensation and associated latent heat release to be highly concentrated near the steam injection zone. In contrast, the CNT model progresses more gradually towards saturation, initially predicting nucleation with smaller bulk condensation rates (and lower heat release) near the injection zone, followed by significant bulk condensation and latent heat release occurring further upstream as fog droplets grow. As a result, the CNT model produces a slightly more spatially distributed heat source.

Despite these variations in the local spread of latent heat release from bulk condensation between the models, their influence on the overall temperature profile and distribution is minor. This is due to the strong convective transport in the inner cylinder region, which quickly redistributes the thermal energy and prevents formation of significant temperature gradients caused by localized heat sources. Consequently, both bulk condensation models yield temperature distribution closely matching with each other and more importantly, with the experimental data.

5.3. Density and buoyancy effects

The temporal variation of gas density distribution along the vessel's central axis for different modeling approaches is illustrated in Fig. 7. The simulations, including bulk condensation models consistently predict lower gas densities within the inner cylinder region compared to the baseline case with wall condensation alone. This reduction in density relates directly to the higher local temperatures induced by the release of latent heat during bulk condensation, as discussed in Section 5.2. Consequently, the bulk condensation simulations exhibit a lighter air gas mixture upstream of the injection zone, which enhances buoyancy forces in those zones. The density will also change due to the local removal of steam, depending on whether that space is replaced by denser nitrogen, lighter hydrogen, or a mixture of the two.

The enhanced local buoyancy forces lead to accelerated flow in regions where bulk condensation reduces the density. This phenomenon is confirmed through the velocity profiles along the central line of the vessel presented in Fig. 8. The bulk condensation models predict significantly higher upward velocities compared to the baseline. reflecting stronger buoyancy forces generated by the latent heat release. To quantify the relative increase in vertical velocity between different modeling approaches, a representative point inside the inner cylinder at y = 4 m and time t = 700 s is selected. At this location, the baseline model predicts a local velocity of U_y = 0.88 m/s, whereas both bulk condensation models yield U_y = 1.61 m/s. This velocity corresponds to an approximate increase of 0.7 m/s in the velocity, representing a 80% enhancement relative to the baseline case. A similar analysis at time

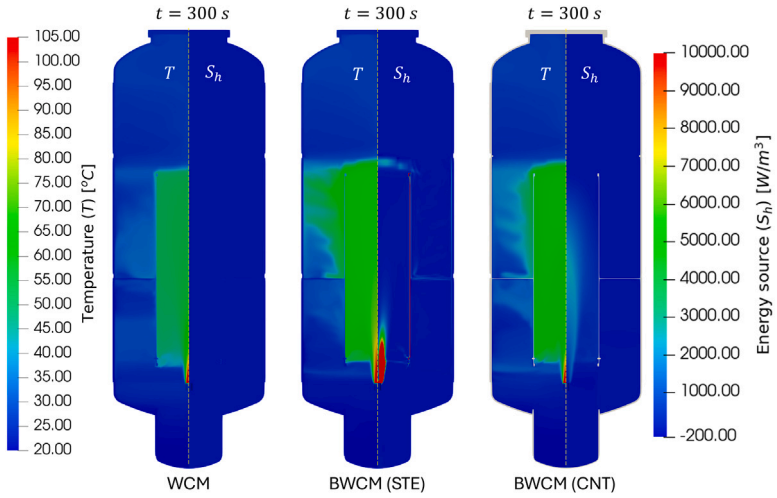

Fig. 6. Comparison of gas temperature (T, left section of each image) and energy source term (S_h, right section of each image) distributions for different modeling approaches at time $t = 300$ seconds.

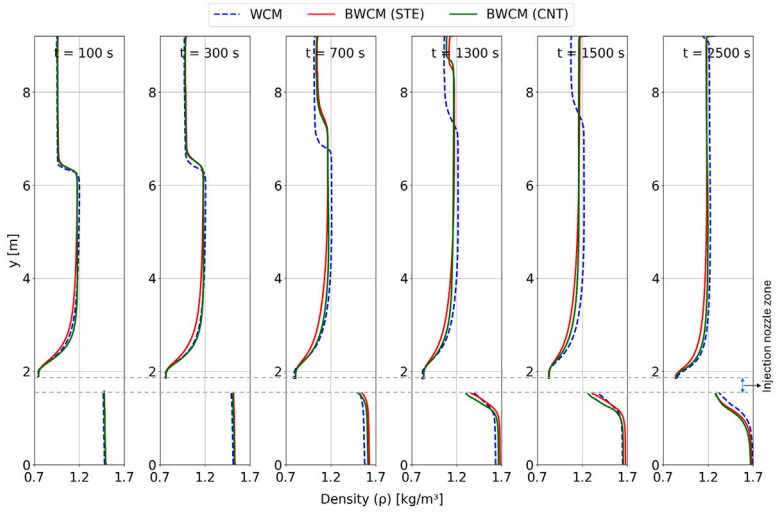

Fig. 7. Comparison of evolution of density distribution along the vessel central axis with different modeling approaches.

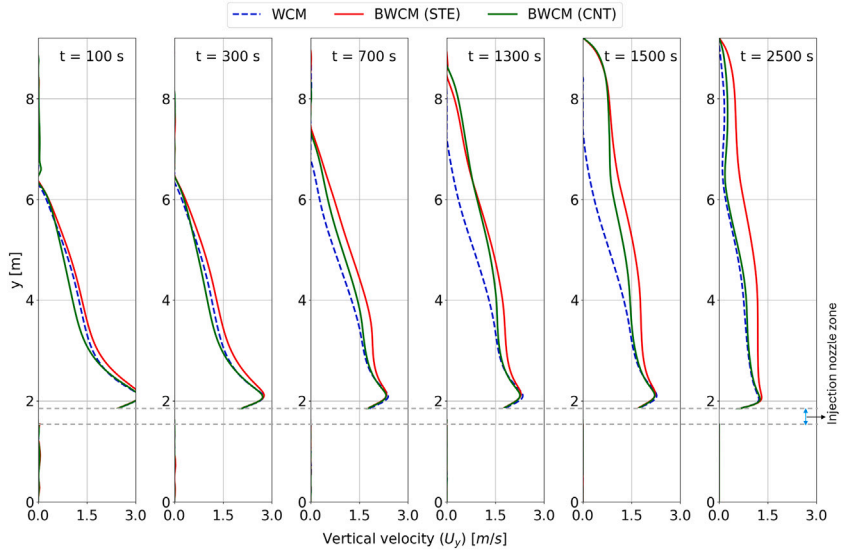

Fig. 8. Comparison of evolution of vertical gas velocity along the vessel central axis with different modeling approaches.

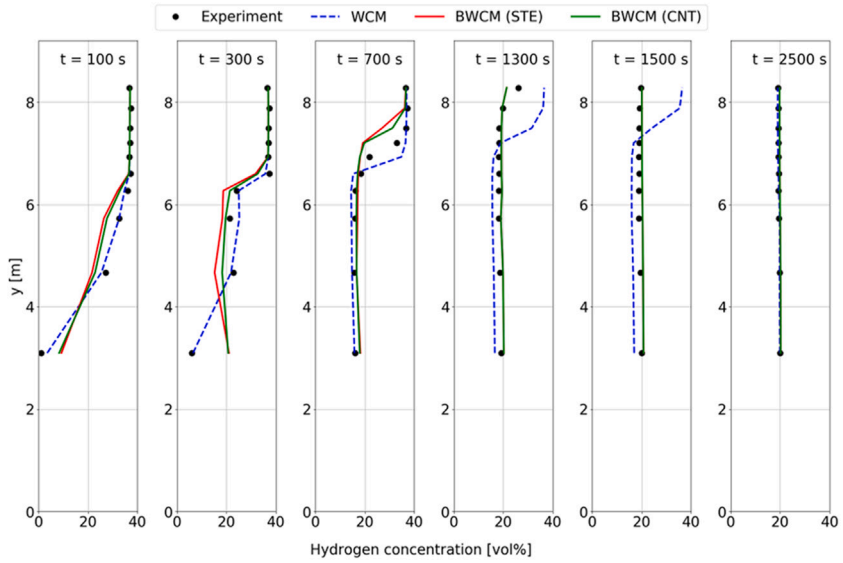

Fig. 9. Comparison of experimental and simulated hydrogen concentration evolution along the vessel height in the annular region.

$t = 100$ s, indicates a velocity enhancement of around 15% at the same vessel location.

There is only marginal difference in density and velocity distributions between the two bulk condensation models across most of the transient. However, during the early stages, the CNT model exhibits slightly lower density difference near the injection zone compared to the STE model. This discrepancy arises because the CNT model predicts a slower build-up of bulk condensation rate, which gradually drives the mixture to saturation condition through nucleation and growth. In contrast, the STE model instantaneously attains saturation temperature equilibrium within the simulation time step, causing immediate condensation and latent heat release near the injection. This initial difference results in slightly higher densities locally for the CNT model compared to STE during initial stages, reducing buoyancy forces correspondingly. However, after around $t = 700$ s, the density profiles for both bulk condensation models converge and become nearly indistinguishable, indicating that their long-term impact on buoyancy and resultant flow dynamics is effectively similar.

5.4. Hydrogen cloud erosion and steam jet penetration

The transient evolution of the vertical hydrogen concentration distribution in the annular region of the vessel is illustrated in Fig. 9. The simulations employing bulk condensation models is able to reasonably replicate the experimentally observed hydrogen distributions throughout the transient, with particularly good agreement during the mid and final stages. Notably, the timing of full hydrogen dissolution, occurring around $t = 1500$ seconds, is accurately and captured only when the bulk condensation effects are considered. In contrast, the baseline simulation with only wall condensation model predicts significant delays in this event, with cloud erosion happening only near $t = 2500$ seconds.

The dissolution process starts when the injected steam plume rises through the inner cylinder and reaches its upper boundary. At this stage, the steam begins to spread laterally into the annular region and flows downward towards the sump region, establishing a weak convective loop. This loop slowly moves upwards towards to the dome and mixes the hydrogen-rich layer, leading to its gradual erosion. Bulk condensation strongly influences this dynamic by enhancing the local buoyancy forces through the release of latent heat, which increase the local gas temperatures and reduces density gradients between the hot steam jet and the hydrogen-rich gas. These amplified buoyancy forces strengthen the convective currents, accelerating hydrogen cloud erosion and steam jet advancement. As the steam front moves upwards and approaches the dome region, the hydrogen gets fully mixed, confirming the timely dissolution prediction by the bulk condensation models. The spatial distributions of hydrogen and steam at $t = 1500$ seconds (Fig. 10) further support these findings. The baseline simulation with only wall condensation model is unable to drive the steam front rapidly, leaving a stratified layer of hydrogen in the dome region, whereas the bulk condensation simulations successfully advanced the steam front faster and completely dissolved the hydrogen cloud.

Furthermore, both STE and CNT bulk condensation models yield nearly same hydrogen concentration fields, indicating that the overall mixing dynamics is not significantly sensitive to the specific bulk condensation modeling approach. This is due to the nearly same net latent heat release by both models in the inner cylinder region, despite some local variations in its distribution.

5.5. Vessel pressure and condensation rate evolution

The comparison of time evolution of vessel pressure between the simulations and experiments is presented in Fig. 11. Simulations incorporating the bulk condensation model predict the overall trend of the pressure evolution well, showing good agreement with the experimental data despite a slight overprediction of around 3%–4%. In contrast, the baseline simulations including only wall condensation exhibit underpredictions and notable deviations from the experiments and fail to capture the correct pressure evolution trend. This discrepancy underlines the vital role of bulk condensation in accurately representing the vessel conditions.

Understanding the vessel pressure evolution requires examining the condensation phenomena within the vessel, since condensation continuously removes a part of injected steam, affecting the pressure rise rate. Fig. 12 illustrates the integral condensations rates and the relative contribution of each condensation mode, predicted by different modeling approaches. It can be observed that the inclusion of bulk condensation leads to an approximately 10% reduction in the wall condensation rates compared to the baseline case. This reduction occurs because some steam condenses in the bulk phase before reaching the walls. However, this decrease is largely compensated by the contribution of bulk condensation rate, resulting in a net condensation rate, which remains nearly same on average as in the baseline simulation. It is important to note that the wall condensation rate refers specifically to steam that condenses directly on wall surfaces, transferring latent heat to the vessel walls. The bulk-condensed droplets that deposit on walls contribute negligibly to wall heat transfer, as their latent heat

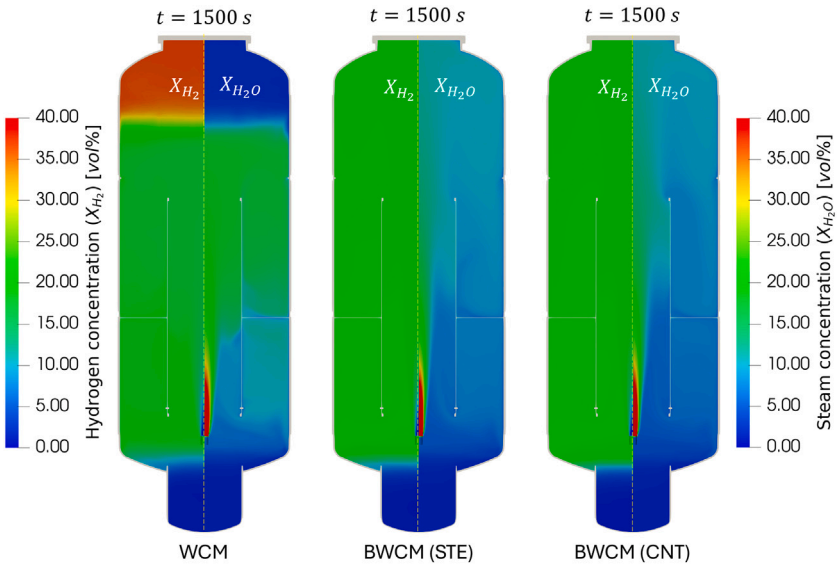

Fig. 10. Comparison of hydrogen concentration (X_{H_2}, left section of each image) and steam concentration (X_{H_2O}, right section of each image) distributions for different modeling approaches at time $t = 1500$ seconds.

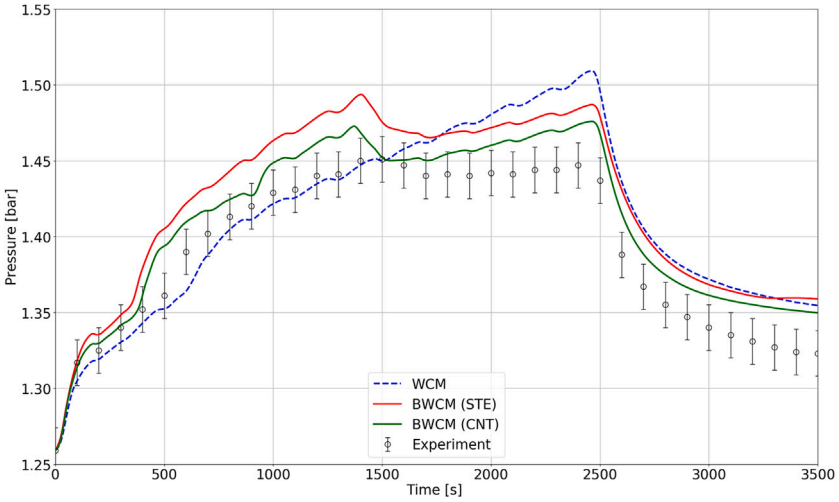

Fig. 11. Comparison of experimental and simulated vessel pressure evolution with time.

has already been released within the gas phase. This relatively small fraction of bulk condensation rate, however, has major influence on the vessel events due to the latent heat released locally and the resulting buoyancy forces.

A closer look into the key time points reveals how the bulk condensation model enhances prediction accuracy. At initial stages ($t = 100$ s), the latent heat from wall condensation is largely transferred to the inner cylinder structure, whereas latent heat from bulk condensation remains in the gas phase, significantly elevating the local gas temperature. This higher temperature early in the transient results in the predicted vessel pressures to be higher than the baseline, aligning it closely with the experimental observation, despite having almost same net condensation rate.

By around $t = 500$ s, the steam plume has cleared the inner cylinder and starts spreading laterally into the annular region. During this brief period, there is a drop in the wall condensation rate caused by the absence of steam-cold wall contact, causing a temporary increase in the pressure rise rate. This is followed by a slight increase in the pressure rise rate, driven by the restoration of wall condensation as the steam comes in contact with the cooler vessel side walls. The bulk condensation model captures this transition accurately, while the wall condensation-only simulation predicts these events delayed by several hundred seconds, around $t = 800$ s.

At around $t = 1500$ s, the steam front reaches the colder upper dome walls, triggering substantial increase in wall condensation rate, large enough to cause a sharp drop in vessel pressure. This sudden elevation in condensation rate is clearly visible in the integral condensation rate curve, which is accurately predicted by the bulk condensation models. The baseline simulation, however, fails to replicate this behavior due to slower steam front progression, which does not reach the dome walls within the injection period ($t = 0$–2500 s). Subsequently, as the dome wall temperature increases gradually, the wall condensation rate diminishes, causing the vessel pressure to start rise again, until the end of steam injection ($t = 2500$) s. Once the injection is stopped, the vessel pressure slowly decreases driven by ongoing wall and bulk condensation.

Although wall condensation remains the dominant condensation mechanism controlling the vessel pressure, accounting for the majority ($\approx 90\%$) of the net condensation rate, the bulk condensation with less than 10% contribution, has proven to have large impact on pressure evolution. This is caused by the latent heat deposition in the carrier gas by bulk condensation, which elevates local temperatures, enhances

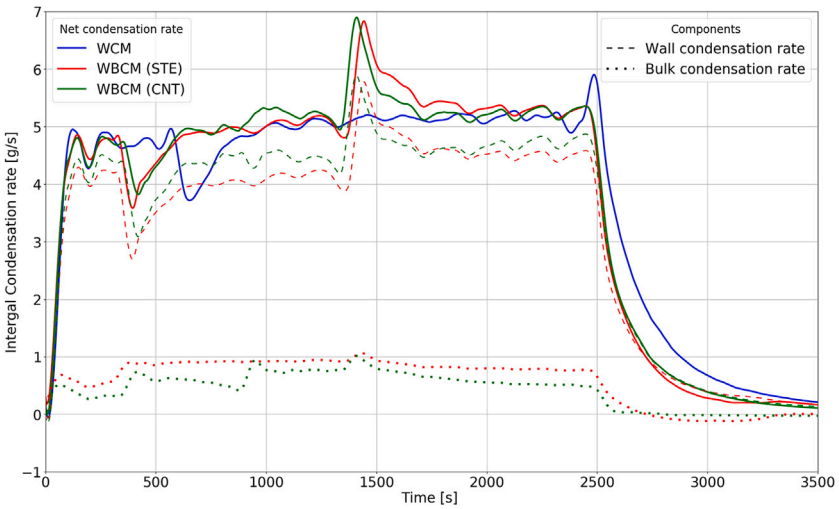

Fig. 12. Quantitative comparison of integral condensation rates with different modeling approaches, highlighting condensation mode-specific contributions to net condensation rate.

buoyancy and accelerates the advancement of the steam front. The bulk condensation models reduced the time required to break the stratified hydrogen layer by approximately 65%, consistent with experimental observations.

The comparison between the bulk condensation models-STE and CNT- reveals broadly similar predictions. The CNT model tends to produce lower bulk condensation rates but with more spread in the inner cylinder region, resulting in marginally faster arrival of steam front at the dome region and moderately lower pressures than the STE model, particularly during the mid to final stages (t = 1300–2500) s. This indicates that even the slight changes in the bulk condensation rates caused by different modeling approaches can have moderate influence on the flow and vessel pressure evolution.

It is worth looking into the pressure and condensation rate evolution during phase 3 when the steam injection ceases. Notable differences are observed in the pressure evolution trends between the bulk condensation model and the experiment, as well as between the two bulk condensation models themselves. The pressure drop rate with STE model is slower than that of the CNT model, which itself is slightly slower than the experimental rate. A detailed analysis of the bulk condensation rates reveals that at around t = 2700 s, the rates evolve to negative values, indicating re-evaporation of residual fog droplets drifting towards warmer vessel regions. This evaporation reduces the rates of pressure rise by adding the steam back to the gas mixture and is key physical phenomenon captured only by fog transport modeling. However, the accuracy of such predictions depends on the precise modeling of droplet size evolution, as drift velocity is predominantly influenced by the droplet diameter. The STE model currently supports only mono-dispersed droplets, with the droplet size set to 20 μm for this study. In contrast, the CNT model allows droplet evolution by growth, which will eventually lead to larger droplet sizes and faster settling of the fog droplets by gravity. Hence, in the simulation with CNT model, the number of droplets available for re-evaporation is lower compared to the STE model, resulting in lower evaporation rates as observed in the bulk condensation rate evolution. A detailed analysis of fog droplet transport and size distribution is presented in Section 5.6. Additional droplet size evolution mechanisms like coalescence can increase the settling velocity and influence evaporation rates and pressure evolution; however, this is beyond the scope of this work.

5.6. Fog droplets transport and size distribution

The time evolution of fog volume fraction within the vessel, as predicted by both bulk condensation modeling approaches, is shown in Fig. 13. At the beginning of steam injection (t = 100 s), fog droplets are concentrated predominantly in the inner cylinder region, coinciding with the zones of active bulk condensation. As the time progresses (t = 300 s), the convection currents transport these droplets upward towards the inner cylinder top exit, after which they flow laterally into the annular region, spreading further and descending. The fog droplets move towards the vessel dome along with the steam front at times around t = 700 s. There is also continuous deposition of droplets on the inner and side walls as well as in the sump, with a higher overall deposition in the CNT case.

Continuous bulk condensation during the steam injection period causes the fog volume fraction within the vessel to increase steadily throughout phase 2. The fog front advances together with the steam front, both reaching the upper dome by around t = 1500 s. At the same time, there is lateral spreading and downward movement of fog within the annulus due to the convection loop and droplet drift. The volume fraction of fog reaches the maximum by the end of steam injection (t = 2500 s) and subsequently reduces during the post-injection period (t = 3000 s) as the droplets are deposited on to the walls and removed from the bulk. The droplet settling occurs even during the injection period, however, it is lower compared to the rate of fog formation.

A notable difference is observed when comparing the two bulk condensation models: the fog volume fraction remains consistently lower in the CNT simulations than in the STE simulations, except once the steam injection has stopped. This distinction arises from the difference in droplet size evolution and corresponding droplet settling velocities. Fig. 14 illustrates the temporal evolution of the fog mean diameter distribution for both models. In the STE approach, a fixed droplet diameter (set to 20 μm) is assumed for droplets, which enabled the droplets to remain suspended for longer duration and slower deposition. In contrast, the CNT model accounts for the nucleation and subsequent growth, which results in significantly larger droplets (in the order of 200 μm). Larger droplets settle more rapidly due to gravity and inertia, leading to greater deposition rates and consequently, lower fog volume fractions in the vessel. This difference highlights a limitation of the STE approach used in this work: the fixed droplet diameter is a modeling parameter that must be calibrated to match experimental observations. Different choice of diameter can considerably influence predicted fog deposition and spatial distribution, necessitating extensive trial-and-error simulations to determine an "optimal" value. In contrast, the CNT approach employed in this work eliminates this diameter calibration by predicting droplet sizes based on nucleation kinetics and condensation growth theory. This approach predicts droplet evolution and subsequent deposition behavior based on physical mechanisms rather

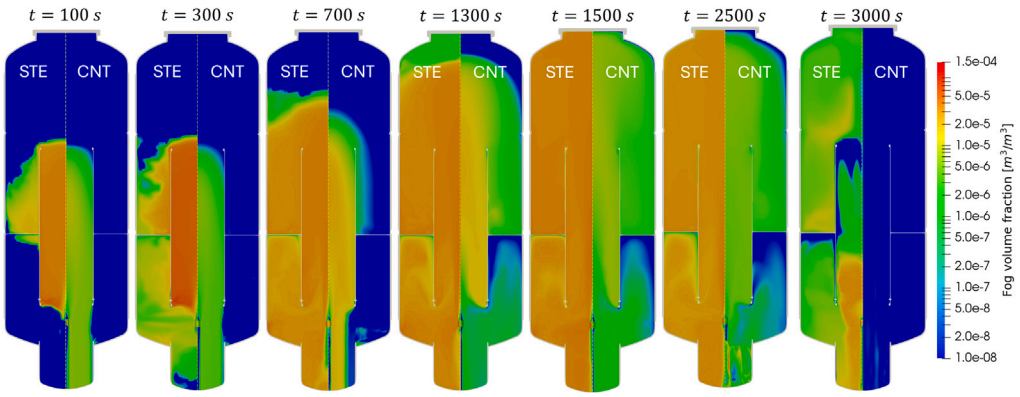

Fig. 13. Comparison of fog volume fraction distribution (logarithmic scale) between different bulk condensation modeling approaches, STE (left section of each image) and CNT (right section of each image) at different time intervals.

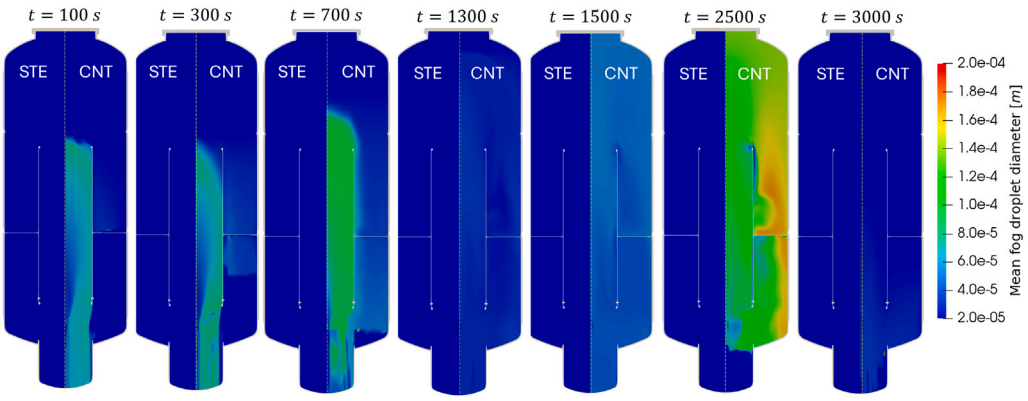

Fig. 14. Comparison of fog droplets mean diameter distribution between different bulk condensation modeling approaches, STE (left section of each image) and CNT (right section of each image) at different time intervals.

than calibration, reducing uncertainty and improving the predictive capability for scenarios beyond the HM2 test case.

In the CNT simulation, the mean droplet size increases in both magnitude and spatial coverage during the initial stages as the steam cloud gradually clears the inner cylinder region. During the mid-stages, the mean diameter decreases due to the deposition of larger droplets and the formation of smaller ones, until the steam front reaches the dome. Once the steam front reaches the dome, the fog droplets become distributed throughout the domain, and continued bulk condensation on these droplets leads to an increase in their mean diameter. After the steam injection stops, further gravitational settling causes a reduction of suspended large fog droplets, with only smaller droplets remaining in the gas mixture. In Section 5.5, the bulk evaporation rates during the post-injection period are higher with the STE approach. This is due to the larger volume fraction of fog retained in the vessel due to slower settling, which is available for evaporation. In contrast, the CNT approach resulted in lower fog droplets available for re-evaporation caused by more rapid settling. It is worth noting that the maximum fog volume fractions observed in the simulations ($1e-4$) approach the range where two-way coupling becomes relevant to account for the droplets momentum transfer. However, this transfer term is estimated to be small (< 1%) compared to the buoyancy term in momentum conservation equation (Eq. (3)), and is neglected in the present study and remains a topic for investigation. Comparison of the fog densities in the injection zone shows that the densities in the present simulation are higher for the STE case (50–100 g/m^3) and lower for the CNT case (10–40 g/m^3), the latter being comparable to the outcomes of benchmark study (Schwarz et al., 2011).

6. Conclusion

This study systematically investigated the impact of bulk condensation on containment thermal hydraulic behavior, especially buoyancy-driven flows and gas mixing in a containment-like vessel, using the *containmentFOAM* CFD package. The results demonstrated that bulk condensation significantly affects buoyancy-driven gas flows by intensifying local latent heat release, thereby enhancing vertical mixing and accelerating the breakdown of stratified light gas layers. By comparing simulations conducted with wall condensation alone, and with two distinct bulk condensation models-the saturation temperature equilibrium (STE) and the classical nucleation theory (CNT) approaches, against experimental data from THAI HM2 test, we demonstrated that inclusion of bulk condensation significantly improves the prediction accuracy. Bulk condensation releases latent heat locally, which elevates the gas temperatures and reduces density, thereby enhancing buoyancy forces that leads to stronger vertical convection currents. These intensified flows accelerate hydrogen cloud dissolution and steam jet penetration, resulting in earlier and more complete mixing consistent with experimental observations.

The vessel pressure evolution, closely related to the condensation processes, was predicted better when bulk condensation was modeled, capturing key pressure transients and timing of pressure change events with 2%–3% of experimental values. Even though bulk condensation contributed less than 10% to the integral condensation rates compared to wall condensation, its influence on the buoyancy forces proved to be critical in accurately simulating the transient vessel behavior. Differences between the two bulk condensation models were minor, mostly limited to initial latent heat release location and droplet size

and volume fraction distributions, with both approaches producing comparable overall mixing and temperature distributions. The CNT model's inclusion of droplet growth and resulting faster settling led to lower fog volume fraction and more realistic re-evaporation behavior in the post-injection phase. This highlights the importance of fog droplet dynamics modeling for improved containment atmosphere predictions. These findings collectively underscore the importance of incorporating bulk condensation model into containment thermal-hydraulics safety codes to enable reliable predictions of atmospheric conditions during accident progression.

The *containmentFOAM* framework demonstrated noteworthy capability in simulating complex multi-interaction phenomena through coupling of multi-species transport, turbulence, wall and bulk condensation and fog transport models. Future work will focus on extending these bulk condensation and fog transport models to include coalescence and breakup mechanics, utilizing population balance modeling frameworks like method of classes. This is expected to further improve the fog volume fraction and size distribution predictions, as well as the settling behavior to enable linking with further physics like aerosol transport. Future investigations could also examine the influence of deviations from ideal gas behavior and radiative transfer, particularly for conditions approaching saturation or strong thermal gradients. Additionally, systematic validation studies at intermediate scales and application to full-scale containment geometries will strengthen confidence in model predictions for severe accident management strategies.

CRediT authorship contribution statement

Allen George: Writing – review & editing, Writing – original draft, Visualization, Validation, Software, Methodology, Investigation, Formal analysis, Data curation, Conceptualization. **Stephan Kelm:** Writing – review & editing, Supervision, Software, Resources, Project administration, Data curation, Conceptualization.

Declaration of competing interest

The authors declare that they have no known competing financial interests or personal relationships that could have appeared to influence the work reported in this paper.

Acknowledgments

The authors express their sincere gratitude to the German Federal Ministry for Economic Affairs and Energy, Germany for funding the national THAI-1 project (No. 150 1326) and to Becker Technologies (Eschborn, Germany) for their meticulous documentation and generous sharing of the THAI experimental data. This open access publication is funded by the Deutsche Forschungsgemeinschaft (German Research Foundation, DFG) - 491111487.

Data availability

The authors do not have permission to share data.

References

Allelein, H.J., Schwarz, S., Fischer, K., Vendel, J., Malet, J., Bentaib, A., Studer, E., Paillere, H., Houkema, M., Sep 2008. International Standard Problem ISP-47 on Containment Thermal Hydraulics - Final Report (NEA-CSNI-R–2007-10). Technical Report, Nuclear Energy Agency of the OECD (NEA).

Antoine, C., 1888. Tensions des vapeurs; nouvelle relation entre les tensions et les températures. Comptes Rendus Séances L'Académie Sci. 107, 681–684, (in French).

Babić, M., Kljenak, I., Mavko, B., 2009. Simulations of TOSQAN containment spray tests with combined Eulerian CFD and droplet-tracking modelling. Nucl. Eng. Des. 239 (4), 708–721.

Celik, I., Zhang, W.M., 1995. Calculation of numerical uncertainty using richardson extrapolation: Application to some simple turbulent flow calculations. J. Fluids Eng. 117 (3), 439–445.

Chung, W., Devaud, C.B., 2008. Buoyancy-corrected k–ϵ models and large eddy simulation applied to a large axisymmetric helium plume. Internat. J. Numer. Methods Fluids 58 (1), 57–89.

Dehbi, A., Janasz, F., Bell, B., 2013. Prediction of steam condensation in the presence of noncondensable gases using a CFD-based approach. Nucl. Eng. Des. 258, 199–210.

Elghobashi, S., 1994. On predicting particle-laden turbulent flows. Applied scientific research. Appl. Sci. Res. 52, 309–329.

Frederix, E., Kuczajd, A.K., Nordlundd, M., Veldmanc, A.E.P., Geurts, B.J., 2017. Eulerian modeling of inertial and diffusional aerosol deposition in bentpipes. Comput. Fluids 159, 217–231.

Fuller, E.N., Schettler, P.D., Giddings, J.C., 1966. New method for prediction of binary gas-phase diffusion coefficients. Ind. Eng. Chem. 58 (5), 18–27.

George, A., Kelm, S., Cheng, X., Allelein, H.J., 2023. Efficient CFD modelling of bulk condensation, fog transport and re-evaporation for application to containment scale. Nucl. Eng. Des. 401, 112067.

Gupta, S., Freitag, M., Liang, Z., Funke, F., Langrock, G., Beck, S., Nowack, H., Bentaib, A., Cantrel, L., Ishikawa, J., Hong, S., Kostka, P., Glover, J., Linde, C., Kotouč, M., Taivassalo, V., 2025. Main outcomes of OECD/NEA THAI-2 project on hydrogen risk and source term investigations: Data application for code validation and containment safety assessment. Nucl. Eng. Des. 436, 113970.

IAEA, 2011. Mitigation of hydrogen hazards in severe accidents in nuclear power plants. In: TECDOC Series, (1661), International Atomic Energy Agency, Vienna.

IAEA, 2015. The fukushima daiichi accident. In: Non-serial Publications, International Atomic Energy Agency, Vienna.

Kaltenbach, C., Laurien, E., 2018. CFD simulation of spray cooling in the model containment THAI. Nucl. Eng. Des. 328, 359–371.

Kampili, M., Vijaya Kumar, G., Kelm, S., Arul Prakash, K., Allelein, H.J., 2021. CFD simulations of stratified layer erosion in MiniPanda facility using the tailored CFD solver containmentFOAM. Int. J. Heat Mass Transfer 178, 121568.

Kanzleiter, T., Fischer, K., Langer, G., 2008. Helium/Hydrogen Material Scaling Test HM-2. Technical Report, Report No. 150 1326 – HM-2 TR, Becker Technologies GmbH, Eschborn.

Kelm, S., Kampili, M., Liu, X., George, A., Schumacher, D., Druska, C., Struth, S., Kuhr, A., Ramacher, L., Allelein, H.-J., Prakash, K.A., Kumar, G.V., Cammiade, L.M.F., Ji, R., 2021. The tailored CFD package 'containmentFOAM' for analysis of containment atmosphere mixing, H2/CO mitigation and aerosol transport. Fluids 6 (3).

Linstrom, P.J., Mallard, W.G. (Eds.), 2025. NIST Chemistry WebBook, NIST Standard Reference Database Number 69. National Institute of Standards and Technology, Gaithersburg, MD, 20899.

Liu, X., Kelm, S., Kampili, M., Kumar, G.V., Allelein, H.J., 2022. Monte Carlo method with SNBCK nongray gas model for thermal radiation in containment flows. Nucl. Eng. Des. 390, 111689.

Manninen, M., Taivassalo, V., Kallio, S., 1996. On the Mixture Model for Multiphase. VTT Publications 288, Technical Research Center of Finland.

Menter, F., Esch, T., 2001. Elements of industrial heat transfer predictions. In: Proceedings of the 16th Brazilian Congress of Mechanical Engineering. COBEM-2001.

Menter, F., Ferreira, J., Esch, T., Konno, B., 2003a. The SST turbulence model with improved wall treatment for heat transfer predictions in gas turbines. Gas turnine congress (International) proceedings. Tokyo. Paper no. 59, Tokyo. Paper (IGTC2003).

Menter, F., Kuntz, M., Langtry, R., 2003b. Ten years of industrial experience with the SST turbulence model. Heat Mass Transf. 4.

Mimouni, S., Lamy, J.S., Lavieville, J., Guieu, S., Martin, M., 2010. Modelling of sprays in containment applications with A CMFD code. Nucl. Eng. Des. 240 (9), 2260–2270.

NEA, 2011. Benchmark Study of the Accident at the Fukushima Daiichi Nuclear Power Plantt. OECD Publishing, Paris.

Nuclear Energy Agency (NEA), OECD, 2025. Best Practice Guidelines for the Use of CFD in Nuclear Reactor Safety Applications – 2024 Update. OECD Publishing, Paris, NEA/CSNI/R(2014)11.

OpenFOAM, 2023. OpenFOAM Foundation version 11. URL: https://www.openfoam.org.

Paladino, D., Kapulla, R., Paranjape, S., Suter, S., Andreani, M., 2022. PANDA experiments within the OECD/NEA HYMERES-2 project on containment hydrogen distribution, thermal radiation and suppression pool phenomena. Nucl. Eng. Des. 392, 111777.

Perry, R., Green, D., Southard, M., 2018. Perry's Chemical Engineers' Handbook, nineth ed. McGraw-Hill Education, New York.

Royl, P., Travis, J., Breitung, W., 2008. Blind GASFLOW Analysis of the hydrogen mixing test HM-2 from the OECD-NEA ThAI-3 project.

Schiller, L., Naumann, Z., 1935. A drag coefficient correlation. Z. Vereines Dtsch. Ingenieure (Z. Ver. Dtsch. Ing.) 77, 318.

Schwarz, S., Fischer, K., Bentaib, A., Burkhardt, J., Lee, J.J., Duspiva, J., Visser, D., Kyttälä, J., Royl, P., Kim, J., Kostka, P., Liang, R., 2011. Benchmark on hydrogen distribution in a containment based on the OECD-NEA THAI HM-2 experiment. Nucl. Technol. 175 (3), 594–603.

Sidorov, A., Yastrebov, A., 2023. Simulation of bulk condensation in a flow of a vapor–gas mixture through a nozzle by CFD-methods using a special computational module. Therm. Eng. 70, 299–310.

Vijaya Kumar, G., Cammiade, L.M., Kelm, S., Arul Prakash, K., Groß, E.M., Allelein, H.J., Kneer, R., Rohlfs, W., 2021. Implementation of a CFD model for wall condensation in the presence of non-condensable gas mixtures. Appl. Therm. Eng. 116546.

Visser, D., Siccama, N., Jayaraju, S., Komen, E., 2014. Application of a CFD based containment model to different large-scale hydrogen distribution experiments. Nucl. Eng. Des. 278, 491–502.

Vyskocil, L., Schmid, J., Macek, J., 2014. CFD simulation of air–steam flow with condensation. Nucl. Eng. Des. 279, 147–157, SI : CFD4NRS-4.

Wilke, C.R., 1950. A viscosity equation for gas mixtures. J. Chem. Phys. 18 (4), 517–519.

Zhang, J., Laurien, E., 2014. 3D numerical simulation of flow with volume condensation in presence of non-condensable gases inside a PWR containment. In: Nagel, W.E., Kröner, D.H., Resch, M.M. (Eds.), High Performance Computing in Science and Engineering '14: Transactions of the High Performance Computing Center, Stuttgart. HLRS 2014, Springer, pp. 479–497.